On the realism of the rain microphysics representation of a squall line in the WRF model. Part I: Evaluation with multifrequency cloud radar doppler spectra observations

On the Realism of the Rain Microphysics Representation of a Squall Line in the WRF Model. Part I: Evaluation with Multifrequency Cloud Radar Doppler Spectra Observations

FRÉDÉRIC TRIDON,[a,e] CÉLINE PLANCHE,[b] KAMIL MROZ,[c] SANDRA BANSON,[b] ALESSANDRO BATTAGLIA,[d] JOEL VAN BAELEN,[b] AND WOLFRAM WOBROCK[b]

[a] *Earth Observation Science, Department of Physics and Astronomy, University of Leicester, Leicester, United Kingdom*
[b] *Université Clermont Auvergne, INSU-CNRS UMR 6016, Laboratoire de Météorologie Physique, Clermont-Ferrand, France*
[c] *National Centre for Earth Observation, University of Leicester, Leicester, United Kingdom*
[d] *Earth Observation Science, Department of Physics and Astronomy, and National Center for Earth Observation, University of Leicester, Leicester, United Kingdom*

(Manuscript received 23 January 2018, in final form 29 April 2019)

ABSTRACT

This study investigates how multifrequency cloud radar observations can be used to evaluate the representation of rain microphysics in the WRF Model using two bulk microphysics schemes. A squall line observed over Oklahoma on 12 June 2011 is used as a case study. A recently developed retrieval technique combining observations of two vertically pointing cloud radars provides quantitative description of the drop size distribution (DSD) properties of the transition and stratiform regions of the squall-line system. For the first time, the results of this multifrequency cloud radar retrieval are compared to more conventional retrievals from a nearby polarimetric radar, and a supplementary result of this work is that this new methodology provides a much more detailed description of the DSD vertical and temporal variations. While the extent and evolution of the squall line is well reproduced by the model, the 1-h low-reflectivity transition region is not. In the stratiform region, simulations with both schemes are able to reproduce the observed downdraft and the associated significative subsaturation below the melting level, but with a slight overestimation of the relative humidity. Under this subsaturated air, the simulated rain mixing ratio continuously decreases toward the ground, in agreement with the observations. Conversely, the profiles of the mean volume diameter and the concentration parameter of the DSDs are not well reproduced. These discrepancies pinpoint at an issue in the representation of rain microphysics. The companion paper, investigates the sources of the biases in the microphysics processes in the rain layer by performing numerical sensitivity studies.

1. Introduction

An accurate representation of precipitation microphysical processes is of primary importance in simulating the state of the atmosphere not only because they determine the properties of the rain falling at the ground but also because, through latent exchanges, they influence the thermodynamics of precipitation systems themselves, and thus their evolution. For example, Morrison et al. (2009) and Bryan and Morrison (2012) showed that the development of trailing stratiform regions in squall lines is sensitive to the representation of rain microphysics through rain evaporation.

Current mesoscale models use bulk microphysics schemes with one (e.g., Kessler 1969; Koenig and Murray 1976; Wilson and Ballard 1999) or more prognostic variables (e.g., Ferrier 1994; Feingold et al. 1998; Thompson et al. 2008; Morrison et al. 2009) to approximate and simulate the particle size distribution. Double-moment schemes are generally found to be more successful than one-moment ones in reproducing observations of various cloud systems (Morrison et al. 2009; Van Weverberg et al. 2012; Igel et al. 2015, and

Supplemental information related to this paper is available at the Journals Online website: https://doi.org/10.1175/MWR-D-18-0018.s1.

[e] Current affiliation: Institute for Geophysics and Meteorology, University of Cologne, Cologne, Germany.

Corresponding author: Frédéric Tridon, ftridon@uni-koeln.de

DOI: 10.1175/MWR-D-18-0018.1

references therein). They are capable of predicting two moments of the size distributions, namely the total number concentration as well as the mass mixing ratio. As such, the double-moment schemes have more flexibility in parameterizing processes like raindrop breakup and self-collection that affect the number concentration but not the mixing ratio (Morrison et al. 2009; Dawson et al. 2010). There is therefore a critical need for new types of observations/retrievals having a sufficient accuracy for evaluating the additional prognostic variables used in microphysics schemes (Morrison and Milbrandt 2011; Van Weverberg et al. 2012).

For example, within an idealized framework, Dawson et al. (2010) studied the differences in evaporation and cold pool properties of a squall line simulated with a single and a triple-moment scheme. The triple-moment scheme showed clear and significant improvements in the cold pool and reflectivity structures of the storms thanks to a more physical representation of microphysics processes such as evaporation rate by allowing vertical variability in the concentration of the drop size distribution (DSD). However, the credibility of such vertical evolution could not be corroborated by observations. In Morrison et al. (2012), significant discrepancies were found between the simulated and observed DSD properties at the ground during a squall line. Misrepresentation of the raindrop breakup, and of the excessive size sorting, particularly acute in two-moment schemes (Wacker and Seifert 2001; Milbrandt and McTaggart-Cowan 2010), were suggested for explaining such discrepancies. However, the sole profiles of rain parameters observed/retrieved for their case study (radar reflectivity and median diameter) were not sufficient for unequivocally determining the cause. Later on, from simulations of an intense mesoscale convective system, Varble et al. (2014b) confirmed that excessive size sorting in double-moment schemes leads to a disproportionate increase of the mean raindrop diameter through the rain layer in both convective and stratiform regions. This complicated their interpretation of the model versus observation differences (i.e., too large mean raindrop diameters and too small concentration parameters close to the surface), in particular when using the Morrison et al. (2009) scheme. Therefore, these studies clearly highlighted the need of more observations of the DSD properties (in particular of the concentration parameter) aloft.

Retrievals of rain microphysics profiles are possible with ground-based radar observations. As in Morrison et al. (2012), polarimetric radars are widely used since they provide retrievals over large areas (Wilson et al. 1997; Bringi et al. 2009); however, only bulk properties of the DSDs are retrieved and with coarse vertical resolution, and the sensitivity to parameters such as drop concentration is generally limited. Another avenue of radar-based rain retrievals exploits the frequency dependence of the interaction between drops and microwave radiation and combines multifrequency vertically pointing Doppler radar observations. In such conditions, retrievals are only possible along a vertical profile but thanks to the relation between raindrop fall speeds and sizes, DSDs can be derived from Doppler spectra. Traditionally, dual-frequency wind profiler methods have been providing accurate retrievals in steady stratiform rain (Cifelli et al. 2000). They suffer from coarse resolution and low sensitivity in light rain but, after more than two decades of progress, they have now reached a level of quality in the drop concentration retrievals that is adequate for profile comparisons with models (Williams 2016). In Varble et al. (2014b), however, this was done only at the 2.5-km level. More recently, techniques exploiting the non-Rayleigh scattering signatures obtained with high-frequency cloud radars have been developed (Kollias et al. 2002; Giangrande et al. 2012). A novel technique formulated in Tridon and Battaglia (2015) and validated in Tridon et al. (2017a) shows great potential in deriving profiles of DSDs at high resolution from the combination of radar Doppler spectra obtained at K_a (35 GHz) and W band (94 GHz).

Multifrequency cloud radar observations have become more and more common only in recent years [e.g., in the framework of the Atmospheric Radiation Measurement (ARM) program (Mather and Voyles 2013)]. The ARM radars are often used in scanning mode and do not record profiles continuously. Multifrequency cloud radar profiles at K_a and W band were exceptionally recorded during the whole duration of a squall line at the Southern Great Plains (SGP) central facility on 12 June 2011 because it was the test phase of the newly available W-band radar. Such observations provide a unique dataset for evaluating microphysical simulations of a squall line.

The overall goal of this work is to get a clear insight into the rain microphysics properties using multifrequency cloud radar retrievals in order to improve their representation in mesoscale models, and, ultimately, to progress in forecasting precipitation. Comparing the results of two different microphysics schemes in the Weather Research and Forecasting (WRF) Model (Skamarock et al. 2008), this study confirms the discrepancies between observed and simulated mean raindrop diameter profiles (Morrison et al. 2012; Varble et al. 2014b) and expands the comparison to raindrop concentration parameter profiles.

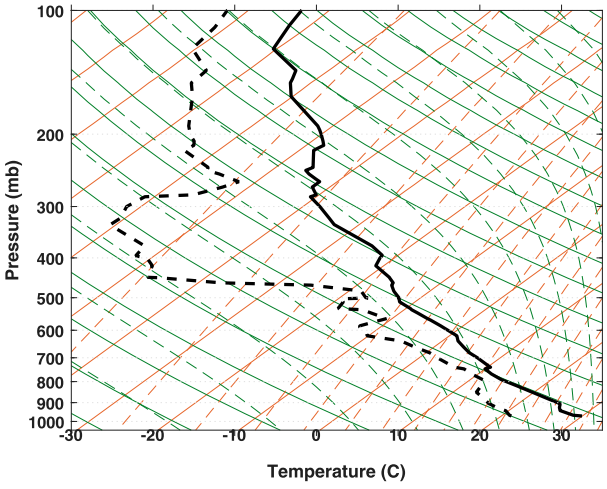

FIG. 1. Thermodynamic sounding from Norman, OK (KOUN), at 0000 UTC 12 Jun 2011.

The paper is organized as follows: section 2 presents the squall-line event under study. Section 3 describes its microphysics properties retrieved by the recently developed dual-frequency cloud radar retrieval and compares them with a more conventional retrieval from polarimetric radars. Section 4 outlines the WRF Model setup, verifies that the general dynamics and thermodynamics conditions are well reproduced in the simulations, and highlight some discrepancies in the rain microphysics properties that will be further investigated in the companion paper, Planche et al. (2019, hereafter Part II). Results are summarized in section 5 while the appendix details the radar retrieval principle and its validation.

2. The 12 June 2011 squall-line event

a. Mesoscale properties

The synoptic conditions on 11 June 2011 reveal the presence of a midlevel trough extending across northwestern United States while a midlevel ridge persisted over portions of the southern plains. Conditions were moderately moist and unstable over Oklahoma, with surface dewpoint temperatures exceeding 23°C and a convective available potential energy (CAPE) of 2502 J kg^{-1} (Fig. 1). Combined with a southeasterly low-level flow advecting moisture northward from the Gulf of Mexico, a midlevel impulse over southwestern Arizona turned toward northern New Mexico. This led to the development of the first thunderstorms in southeastern Colorado at 1900 UTC 11 June 2011, which moved southeastward toward Oklahoma and then became an organized mesoscale convective system resulting in more than 50 mm of rain accumulation over large parts of Oklahoma and Kansas (Fig. 2).

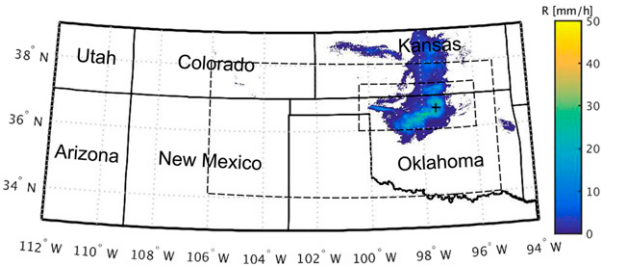

FIG. 2. Instantaneous rainfall rates derived from the Multi-Radar Multi-Sensor (MRMS) product (Kirstetter et al. 2015) illustrating the extent of the MCS at 0600 UTC 12 Jun 2011. The ARM SGP Central Facility location is indicated by the plus symbol. The dashed boxes indicate the two innermost domains used in the WRF simulations.

b. Observations at SGP

The resulting squall-line system passed over the Southern Great Plains (SGP) ARM Central Facility (320 m MSL) from 0500 to 0900 UTC 12 June 2011, producing heavy rain peaking at 100 mm h^{-1} at 0540 UTC and followed by more than 2 h of moderate stratiform rain (Fig. 3). Then, the system moved to southwestern Missouri where it dissipated at 2030 UTC 12 June 2011. The nearby Weather Surveillance Radar-1988 Doppler (WSR-88D) at Vance, Oklahoma (KVNX, frequency of 2.8 GHz, wavelength of ≈10 cm), observed the structure and the evolution (Figs. 4a,d,g) of the squall-line system, characterized by three typical regions with marked differences in the intensity of the reflectivity.

A large suite of radar profiling observations is available at the ARM SGP site: the K_a-band ARM zenith radar (KAZR; Matthews et al. 2011), the W-band scanning ARM cloud radar (WSACR; Matthews et al. 2005), and the ultrahigh-frequency (UHF) radar wind profiler (RWP; frequency of 915 MHz, wavelength of 33 cm, Muradyan and Coulter 1998) reconfigured in precipitation mode (Tridon et al. 2013b). All three radars captured the whole evolution of the squall line as it was passing over the site (Figs. 5 and A1). In particular, the KAZR and WSACR recorded the full profiles of Doppler spectra, key inputs to the dual-frequency rain retrieval used in this work, the rationale of which is detailed in the appendix.

In line with rain rate measured at the ground, the time evolution of the RWP reflectivity Z_{RWP} (Fig. 5a) presents a clear contrast between the leading mature convective region (CR) with multiple columns of high reflectivity corresponding to heavy precipitation (from 0515 to 0600 UTC) and the trailing stratiform region (SR) with the characteristic bright-band (BB)

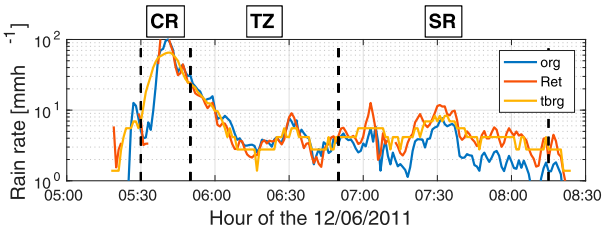

FIG. 3. Evolution of the rain rate measured by the ARM SGP optical gain gauge (org) (blue line), the ARM SGP tipping-bucket rain gauge (tbrg) (yellow line), and retrieved from the lowest radar observations at 700 m MSL (orange line).

highlighting the 0°C isotherm where ice melting occurs (from 0645 to 0815 UTC). As common in squall-line systems (Biggerstaff and Houze 1991), these two regions are separated by a transition zone (TZ) of lighter precipitation with lower reflectivity in rain and a slightly less marked BB (from 0600 to 0645 UTC). The corresponding Doppler velocity (Fig. 5b)—sum of the vertical air motion and the mean reflectivity weighted velocity of hydrometeors—highlights the contrast between ice crystals and raindrop fall velocities in the SR and the TZ, while some strong and alternating updrafts and downdrafts are present in the CR up to 12 km.

Thanks to their peculiar mesoscale structure with these three regions of disparate microphysical regimes, squall lines have been widely used for analyzing the variability of the DSDs (Maki et al. 2001; Uijlenhoet et al. 2003) and to assess models performances against observations (Bryan and Morrison 2012; Morrison et al. 2012, 2015). Figure 6a shows the time evolution of the DSDs retrieved at the lowest range gate (300 m AGL) from the combination of KAZR and WSACR observations (details in the appendix). No disdrometer observations were available for this particular case study. Nevertheless, a comparison of the corresponding rain rate with collocated rain gauges (Fig. 3) shows good consistency over the wide range of rain rates observed during this event. Interestingly, the optical rain gauge underestimates the rain rate in the SR (i.e., between 0700 and 0815 UTC). This suggests that its calibration may be inappropriate to the specific DSD properties

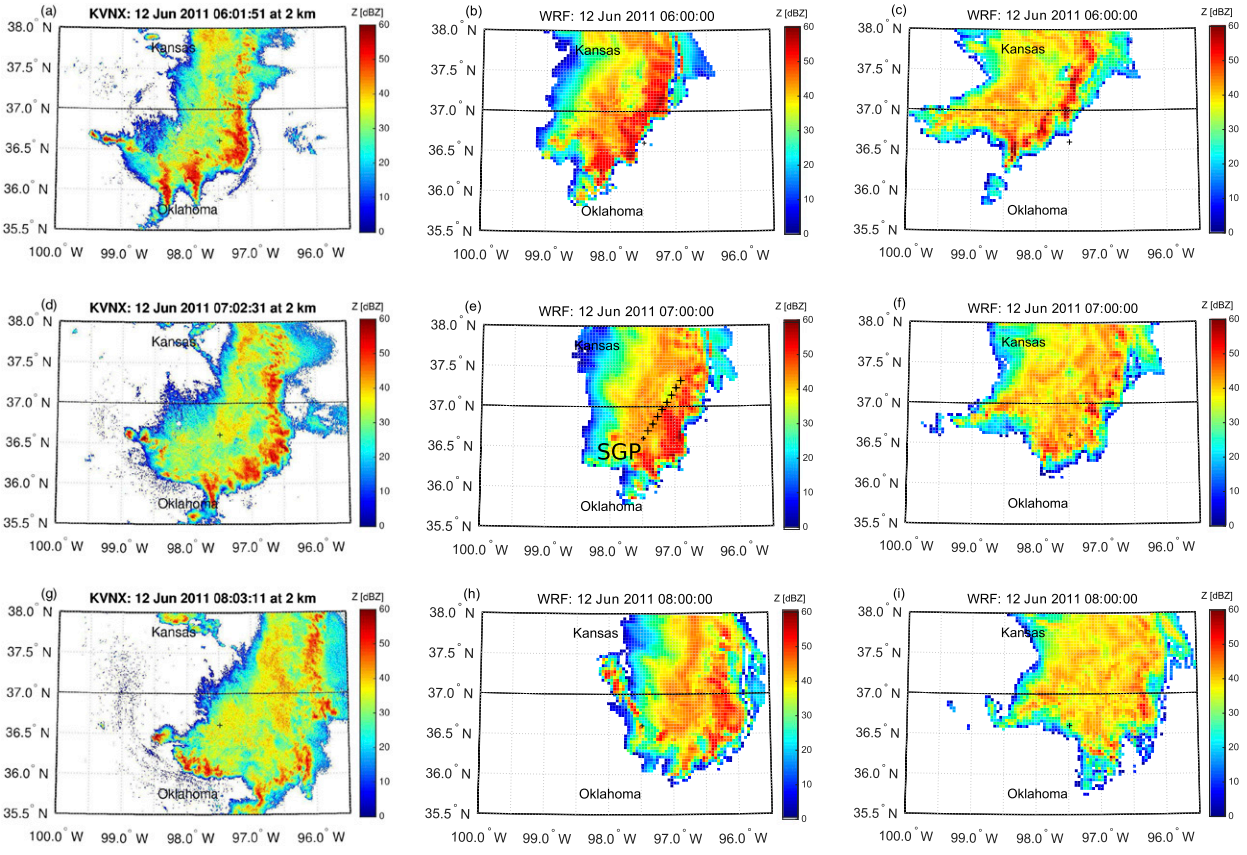

FIG. 4. Evolution of the 2 km MSL radar reflectivity field at 0600, 0700, and 0800 UTC obtained by (a),(d),(g) the KVNZ radar and (b),(e),(h) with the MORR-CTL and (c),(f),(i) THOM-CTL simulations. The cross in the middle of all panels shows the SGP site used to derive the cross sections of the simulations in Fig. 11, and the eight crosses in (e) show the positions used for deriving the additional cross sections in Figs. S1 and S2.

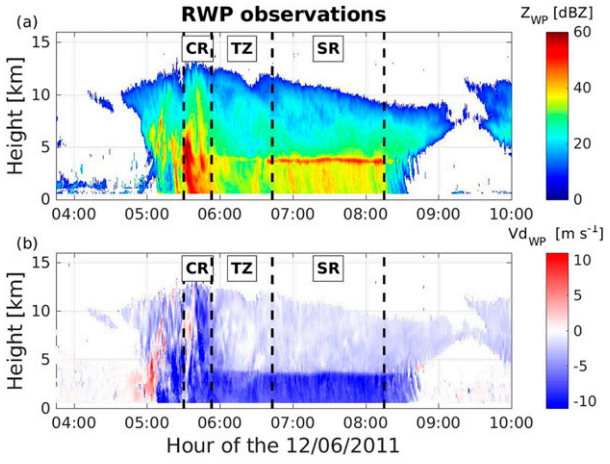

FIG. 5. Time–height evolution of the (a) ARM radar wind profiler (RWP) reflectivity Z_{RWP} and (b) mean Doppler velocity V_d. Dashed vertical lines indicate the limits of the squall-line regions determined manually from the rain reflectivity. Upward velocity is defined as positive.

encountered in the SR. Aloft, the quality of the retrievals is demonstrated in the appendix thanks to quantitative comparisons with the RWP reflectivity observations.

The DSD characteristics are in agreement with the standard interpretation of the microphysical processes involved in squall lines (Biggerstaff and Houze 1993; Houze 1993; Braun et al. 1996). In the CR, the growth associated with convection tends to produce the largest hydrometeors and a wide range of raindrop sizes (median D_0 and maximum D_{max} diameter reach 4 and 7 mm, respectively, Fig. 6). The possible presence of a reflectivity minimum and weak bright band in the TZ (Fig. 5a) is well known and is caused by a smaller degree of aggregation occurring above the melting layer compared to the SR (Biggerstaff and Houze 1993; Houze 1993; Braun et al. 1996). These studies suggested that this can be due to a midlevel downdraft and/or to a predominant presence of convectively generated dense ice particles, which are less efficient to aggregate than the vapor-grown ice crystals found in the SR. Another possibility could be that not much ice is sedimenting there, because large and dense particles have already fallen out while smaller or less dense particles are detrained high in the troposphere so that they do not reach the melting level until they are well behind the convective line. In Fig. 6, this results in smaller drops and a narrow DSD in the TZ (D_0 and D_{max} as small as 1.2 and 2.5 mm, respectively) compared to the SR (D_0 and D_{max} fluctuating around 2 and 5 mm, respectively).

A novelty of this study is the availability of the spectral DSD evolution aloft (Fig. 6b). Only the TZ and the SR vertical evolution can be described because of the full extinction of cloud radar signals in the CR. While the vertical evolution of the DSD is significant (e.g., D_0 and D_{max} generally increasing toward the ground), the differences between the TZ and the SR DSDs aloft are already evident with smaller but more numerous drops in the TZ. With the high-resolution description of the vertical evolution of the rain properties, these two periods of distinct rain microphysics, both persisting over about 1 h, are a perfect test bed to assess if these observed rain microphysics are well reproduced in the mesoscale simulations.

3. Retrieved rain microphysics from radar observations

Before evaluating the rain microphysics representation in WRF, conventional polarimetric radars retrievals are compared with the recently developed multifrequency cloud radar retrievals. The retrieved parameters of the DSD are the mean volume diameter D_m and the concentration parameter N_0^* (defined as the intercept parameter of the corresponding exponential DSD with the same liquid water content and D_m regardless of the shape of the observed DSD, Testud et al. (2001)). Such parameters are widely used for rainfall studies because their definition is independent of the shape of the DSD, $N(D)$, and they are predominantly weighted by drops that contribute the most to the mass content. Their general expressions as function of $N(D)$ are

$$D_m = \frac{M_4}{M_3}, \tag{1}$$

$$N_0^* = \frac{4^4}{\Gamma(4)}\frac{M_3^5}{M_4^4}, \tag{2}$$

where M_i is the ith-order moment of $N(D)$ (Testud et al. 2001).

a. Polarimetric radar retrieval

Polarimetric radars enable to retrieve parameters of rain DSDs over wide areas. When volume scans are performed, vertical profiles can also be reconstructed at any location. Here, the focus is on the retrievals made above the SGP site by the KVNX radar, which is located at a distance of 59 km from SGP. With the highest elevation angle (20°) pointing above the top of the system and the lowest elevation angle (0.5°) reasonably close to the ground (700 m AGL), this is likely to be within the range of ideal distances for looking at vertical profiles with WSR-88Ds. However, this results in only five elevation angles covering the 3-km-thick rain layer, with a

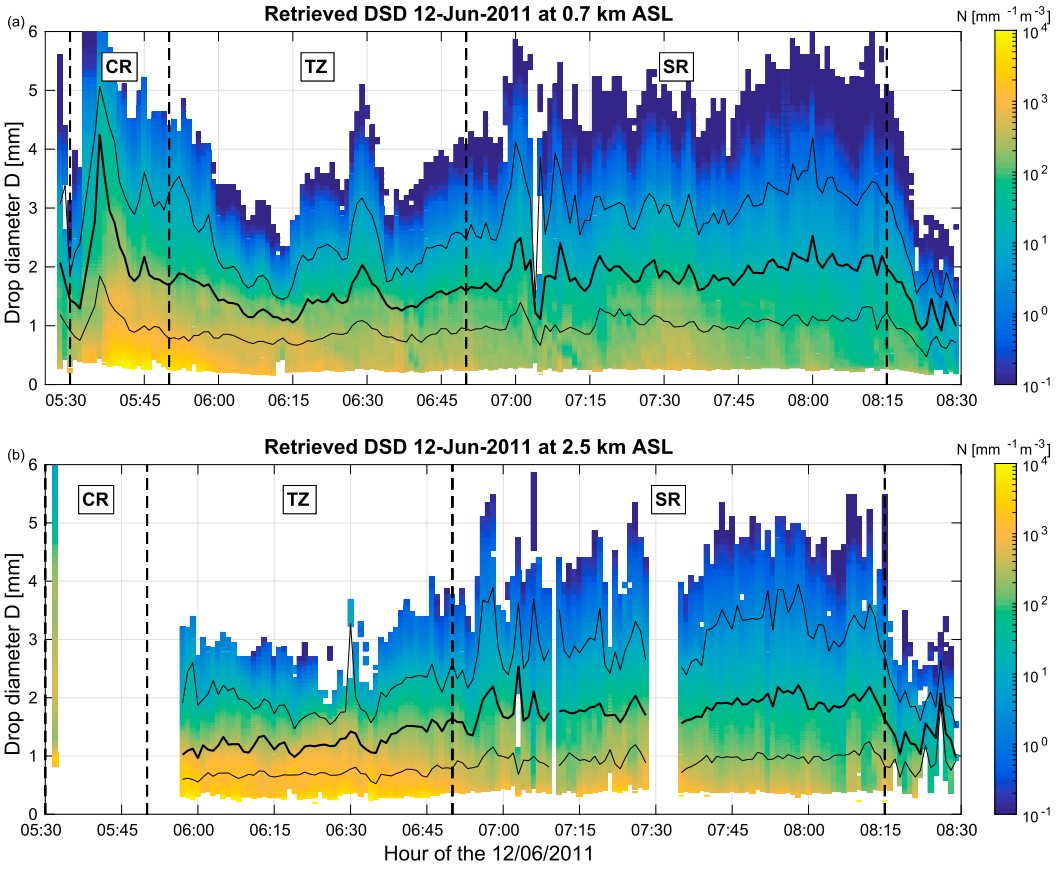

FIG. 6. DSD time evolution retrieved at (a) 0.7 and (b) 2.5 km MSL from the combination of Doppler spectra observed by K_a- and W-band radars (details in the appendix). The black lines are the diameters corresponding to the 10th, 50th (i.e., median diameter D_0), and 90th percentiles of the total rain volume.

resulting sampling vertical resolution of roughly 500 m but with the effective resolution due to the beamwidth being even worse (1 km).

The algorithm used to retrieve the DSD parameters from polarimetric radar observations is described in Bringi et al. (2015). It is a statistical retrieval based on disdrometer observations taken during the Midlatitude Continental Convective Clouds Experiment (MC3E) field campaign (Jensen et al. 2016), which took place around the SGP site during the two months before this squall-line event. The parameters retrieved by this technique are N_0^* and the median mass diameter D_0 with a temporal resolution of 5 min (i.e., the time taken by KVNX to perform a volume scan). Since D_m is directly computed from the moments of the DSD, it is preferred to D_0 in the rest of this study. Accordingly, by assuming that the DSD is well represented by the normalized gamma function (Testud et al. 2001):

$$N(D) = N_0^* f(\mu)(D/D_m)^{\mu} e^{-\Lambda D}, \tag{3}$$

where Λ and μ are the slope and shape parameters and

$$f(\mu) = \frac{(4+\mu)^{4+\mu}}{4^4} \frac{\Gamma(4)}{\Gamma(4+\mu)}, \tag{4}$$

the term D_m can be derived from $D_m = D_0\,(4 + \mu)/(3.67 + \mu)$. Since μ is not a retrieved parameter, a fixed value $\mu = 3$ is chosen within the range -2 to 5 typically assumed in retrieval studies (Tian et al. 2007; Grecu et al. 2016; Mason et al. 2017). Small differences in D_m are found if μ is derived by using a climatological μ–Λ relation (Williams et al. 2014).

Despite its coarser temporal and vertical resolution, the KVNX reflectivity above SGP (Fig. 7a) is in good agreement with that of RWP, depicting a clear convective column around 0530 UTC, and a reflectivity minimum between 0600 and 0645 UTC. As expected, the retrieved D_m (Fig. 7b) is maximum in the CR (≈2.2 mm), minimum in the TZ (≈1.2 mm), and intermediate in the SR (≈1.6 mm). Such values are very close to what has been found in the squall line described in Morrison et al. (2012), but the contrast between each period is not as marked as that derived by

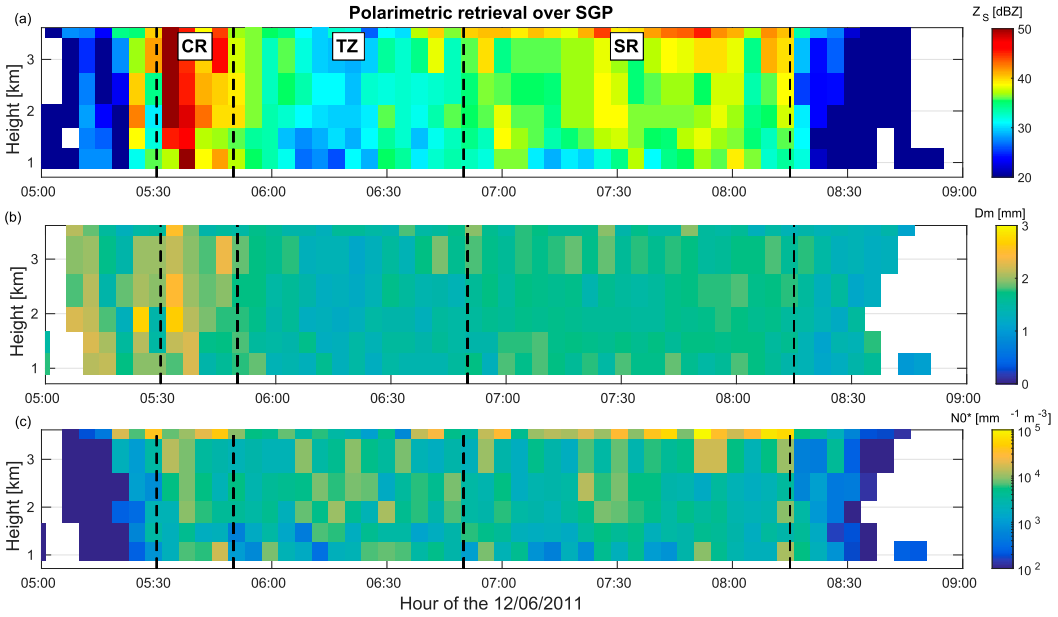

FIG. 7. Time evolution of (a) KVNX reflectivity, (b) D_m, and (c) N_0^* profiles reconstructed above the SGP site.

the multifrequency retrieval (Fig. 8). On the contrary, N_0^* is fairly noisy and its TZ maximum, commonly found in disdrometer observations (Maki et al. 2001; Uijlenhoet et al. 2003), is not reproduced. Similarly, it is difficult to identify any clear vertical variation neither for D_m nor for N_0^*. These limitations are related to the fact that polarimetric retrievals work best for heavier rain where the presence of large drops enhances the polarimetric signals.

b. *Dual-frequency cloud radar retrieval*

The combination of vertically pointing K_a- and W-band radars enables the retrieval of DSD profiles. In fact, at these frequencies, the interaction with raindrops depends on the radar frequency [see Tridon et al. (2017a) and the appendix for details]. Examples of time evolution of the retrieved DSD at 0.7 and 2.5 km MSL were shown in Fig. 6. From each DSD, any rain microphysics parameter can be computed, and Fig. 8 presents the time evolution of D_m and N_0^* rain profiles, as well as rain mixing ratio (q_r) profiles in order to facilitate later comparisons with modeling results (section 4d). Vertical wind (w) profiles are also retrieved with an accuracy of about 10 cm s^{-1} (Tridon et al. 2017a). In case of heavy rain, the signal of cloud radars can be fully attenuated rendering the dual-frequency retrieval inapplicable (e.g., see the region above 1 km in the CR and above 2 km around 0730 UTC). Note that the retrieval assumes that only rain is present in the radar volumes, which is certainly valid at least for the TZ and the SR where reflectivity is lower than 45 dBZ.

As expected from the DSD time evolution (Fig. 6), the dual-frequency retrieval clearly features the three squall-line regions with consistent properties in each regions, both in terms of D_m and N_0^* (Figs. 8a,b). In agreement with previous disdrometer observations (Maki et al. 2001; Uijlenhoet et al. 2003), low D_ms and large N_0^*s are found in the TZ, while no particular differences are found for mixing ratios (Fig. 8c). As was already shown by Williams (2016) for another squall line, there is some significant vertical variation, with a clear decrease of N_0^* and a slight increase of D_m toward the ground. While the case in Williams (2016) has a TZ of only 5 min long—too short to depict any clear vertical variation—the high resolution of the current retrieval and the longer TZ duration of this case study enable a more quantitative investigation of the vertical evolution in the TZ.

c. *Interpretation and comparison of averaged retrieved profiles*

For an easier interpretation of the vertical evolution of the DSD, D_m and N_0^* are averaged over the different periods of the squall line as defined in Fig. 5. Since the dual-frequency profiles are not complete in the CR, only the TZ and the SR are further analyzed. The rain evolution as observed by radars is not in steady state. Since the averaging time is much longer than the typical fall time of the drops (according to the fall velocity–diameter relation of Atlas et al. (1973), drops of 0.8 and 3 mm—roughly corresponding to the 10th and 90th percentile of the DSD mass in Fig. 6—fall through the

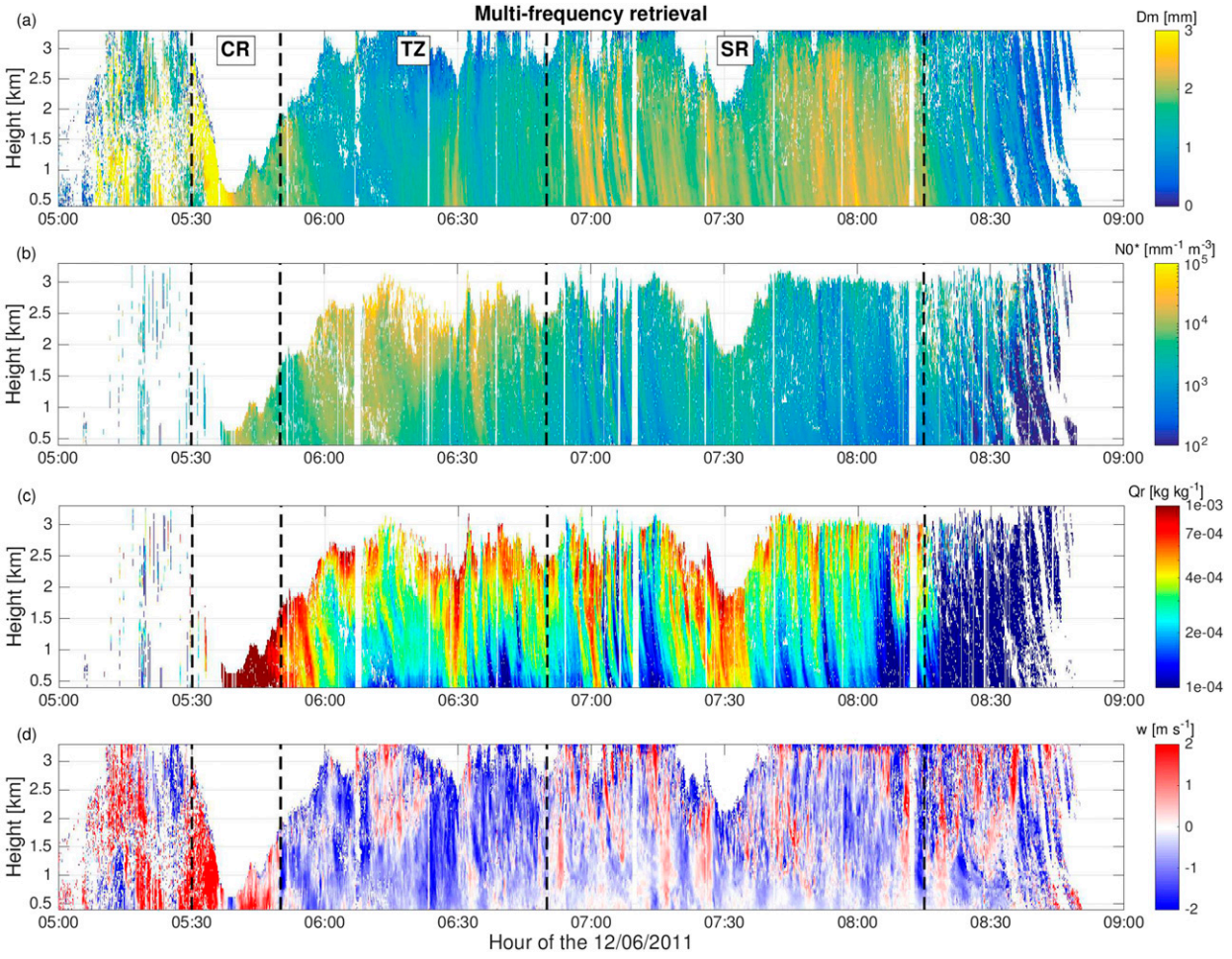

FIG. 8. Time–height evolution of some of the retrieved parameters: (a) mean volume diameter D_m, (b) concentration parameter N_0^*, (c) rain mixing ratio q_r, and (d) vertical wind w. The vertical lines indicate the three different periods of the squall line determined from Fig. 5.

2.5-km layer under study in 13 and 5 min, respectively), the averaged vertical profile can be considered as the vertical evolution of rainfall in an average state.

Looking at the dual-frequency retrieval (black lines and gray shading in Fig. 9), D_m increases toward the ground for both the TZ and the SR periods but at faster rate in the TZ, while N_0^* decreases in the TZ and is almost constant in the SR. For heavy rain and when breakup and self-collection of raindrops are the dominant microphysics processes (i.e., with negligible condensation/evaporation and under no wind shear), many theoretical studies (Hu and Srivastava 1995; McFarquhar 2004) have suggested that the DSD tends toward an equilibrium with an exponential tail at large sizes with a fixed slope. Numerous observations suggest a slope of 2.0–2.2 mm^{-1} (i.e., a D_m of roughly 1.8–2 mm under the assumption of an exponential DSD). For moderate rain rates similar to those under consideration in this work, Barthes and Mallet (2013) have shown that, while the equilibrium DSD is never reached, D_ms of the simulated DSDs always evolve toward the equilibrium value. The SR DSD is closer to this equilibrium already at the highest level of the retrieval just below the melting layer (lying between 3.5 and 4.1 km). This is probably a direct consequence of the snow size distribution properties, rather than a quick evolution of the SR DSD toward the equilibrium in the few hundred meters thin rain layer just below the melting layer where the retrieval is not applicable. Conversely, with a higher concentration of drops (and hence more drop interactions), it seems plausible that the TZ DSD evolves more quickly toward the equilibrium than the SR DSD between 3 and 1 km. Therefore, even though this is an oversimplified interpretation, the dual-frequency retrieval features fine details of the DSD vertical profile in this squall line,

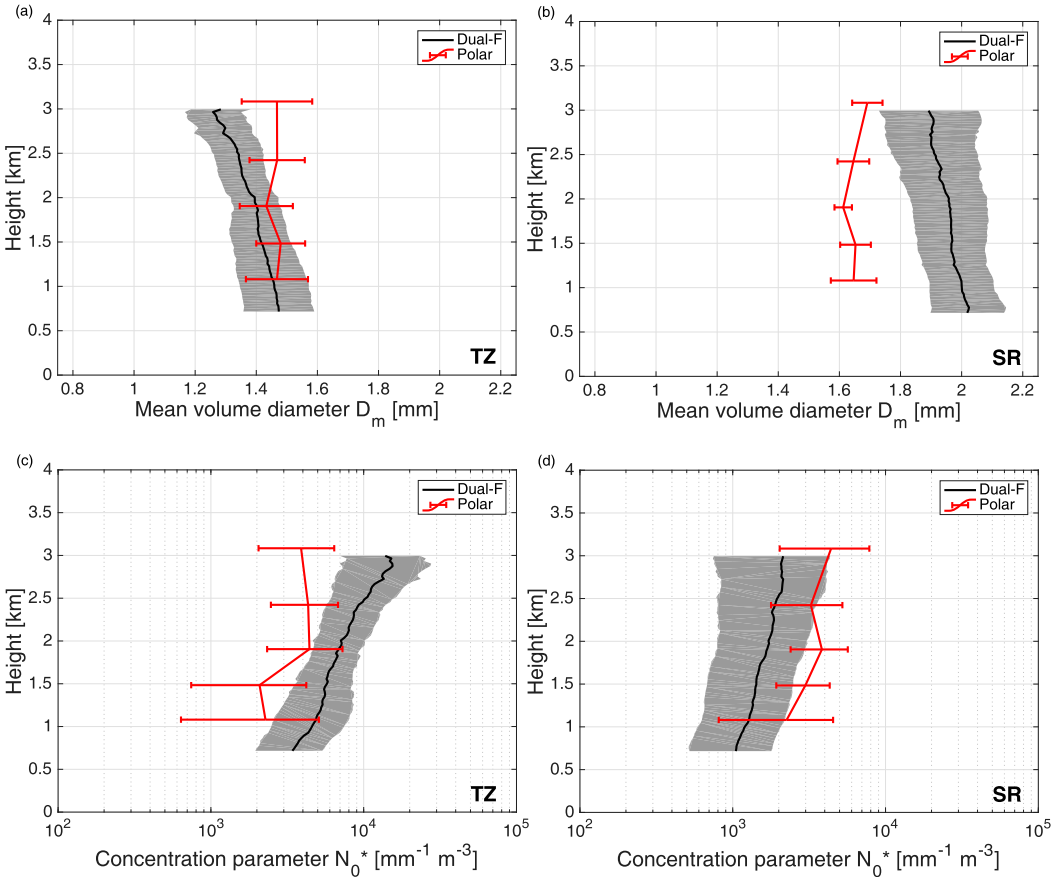

FIG. 9. Averaged profiles of (a),(b) D_m and (c),(d) N_0^* obtained with the dual-frequency (black lines) and polarimetric (red lines) retrievals for the (a),(c) TZ and (b),(d) the SR periods. Gray shading and error bars show the standard deviation of the retrieved parameters within the corresponding period.

which are compatible with our common understanding of DSD evolution.

Averaged retrievals from the polarimetric radar (red lines end error bars in Fig. 9) differ significantly from the dual-frequency retrieval. This suggests that the polarimetric retrieval smooths D_m variations, both in the vertical and between the TZ and the SR region. Contamination by the bright band can explain some of the discrepancies at 3 km (a closer look at Fig. 7 suggests that Z and D_m seem to be indeed often larger at this level). The averaged N_0^* profile of the polarimetric retrieval for the TZ and the SR are very similar and they lie in the middle of the range of the dual-frequency retrieval, suggesting again that the polarimetric retrieval smooths the DSD variations. Several reasons can explain why the polarimetric retrieval provides limited details of the rain microphysics:

- Since the profile is reconstructed from a volume scan, the vertical resolution is very coarse.
- Such moderate rain rates (in particular in the TZ) do not correspond to the range of best performances for polarimetric radars retrievals, and noisy measurements of reflectivity and differential reflectivity can only lead to noisy retrievals.
- The DSD parameters are retrieved from the polarimetric radar observables based on an algorithm adjusted from few convective case studies (Bringi et al. 2015). The bias observed in the SR may be due to the fact that the derived statistical relations are not so well representative of stratiform rain.
- The retrieval quality can be affected by nonuniform beam filling (Ryzhkov 2007) because of large sampling volumes (the polarimetric radar has a much larger beamwidth than the cloud radars and retrievals are made at a much farther distance from the radar).

The polarimetric radar retrievals are unrivaled for providing the DSD properties over wide areas, including heavy rain, and can be used for various application like assimilation in numerical weather prediction models or assessment of mesoscale simulations. However, these results suggest that, when detailed observations are needed for microphysics processes studies

[like in Morrison et al. (2012)], it would be advantageous to rather use retrievals from vertically pointing cloud radars. While the counterargument could be centered on their limitation to moderate rain rates and their representativeness, profilers observations have indeed been successfully used for model evaluation in some previous studies (Varble et al. 2014b).

This is the first time that the polarimetric and dual-frequency cloud radar retrieval are being compared: while the comparison should be extended to a much larger dataset (including comparisons with disdrometer), this work suggests that the accuracy of polarimetric retrieval may not be sufficient when looking at finescale microphysics properties.

4. Numerical simulations of the squall-line system

a. Model description

Simulations of the squall line were done using the compressible, nonhydrostatic Advanced Research version of the Weather Research and Forecasting (WRF) Model version 3.6.1 (Skamarock et al. 2008). For this study, the simulations use the following set of parameterizations: the longwave and shortwave radiation follow, respectively, the RRTM scheme based on Mlawer et al. (1997) and the Dudhia scheme (Dudhia 1989); the surface layer scheme [the revised MM5 Monin–Obukhov scheme described in Jiménez et al. (2012)]; the Unified Noah land surface model (Chen and Dudhia 2001); the YSU boundary layer (Hong et al. 2006) and the microphysics schemes either from Morrison et al. (2009) or from Thompson et al. (2008).

A two-way nesting configuration is used with three domains (represented in Fig. 2) at increasing horizontal resolution: 12, 4, and 1 km. In the horizontal, the domain sizes are, from the outermost to the innermost domain, 1656 km × 600 km, 1008 km × 456 km, and 384 km × 152 km. For the three domains, 72 levels, not linearly spaced to give more levels near the surface, are employed in the vertical with the model lid at about 20 km (mean vertical grid spacing equal to 250 m). The larger domain is initialized at 0000 UTC 11 June 2011 and forced every 6 h with the ERA-Interim operational reanalyses (Dee et al. 2011) from the European Centre for Medium-Range Weather Forecasts. The different simulations last 36 h.

The model settings described above provide control simulations (in contrast with the sensitivity studies performed in Part II), which will be referred to as MORR-CTL and THOM-CTL for Morrison et al. (2009) or Thompson et al. (2008) microphysics schemes, respectively.

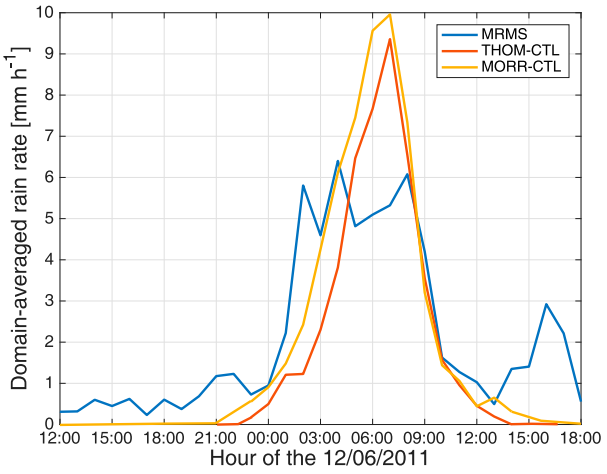

FIG. 10. Temporal evolution of the innermost domain-averaged rain rate at the surface retrieved from observations and in THOM-CTL and MORR-CTL from 1200 UTC 11 Jun 2011.

b. Evolution and structure of the simulated squall line

In WRF, the radar reflectivity is calculated assuming Rayleigh scattering (radar wavelength much larger than the hydrometeor sizes) via the integration of the size distributions of each hydrometeor category (Smith 1984). It can therefore be compared with low-frequency rain radars such as the WSR-88D and the ARM UHF RWP. Note, however, that important assumptions are made in WRF on the mass–size relation of ice species and on the shape of hydrometeors, which are considered spherical. This is why no quantitative or statistical comparison are attempted: only significant differences (of the order of 10 dB) are discussed in the following.

Comparison of the temporal and spatial evolution of the modeled reflectivity (with the KVNX S-band radar reflectivity, Fig. 4) and of the temporal evolution of the innermost domain-averaged surface rain rate [with the hourly instantaneous precipitation retrieved from the S-band rainfall radars of the U.S. NEXRAD network (Kirstetter et al. 2015); Fig. 10] show that the extent and timing of the squall line are fairly well reproduced. A delay of about 1 h is visible, but this is rather small knowing that the system is initiated at around 1900 UTC 11 June 2011 in southern Colorado (i.e., several hundreds of kilometers away).

Figure 4 also shows that the internal structure is reasonably well reproduced with a leading convective line followed by trailing stratiform precipitation. One notable difference, however, is that the transition zone is only somewhat visible in the MORR-CTL simulation and nonexistent in the THOM-CTL simulation. Furthermore, some major differences are observed in a more quantitative sense: 1) the average rain-rate peak is significantly overestimated by both simulations; 2) the

reflectivity of the convective line is rather well reproduced in THOM-CTL (even though this is slightly masked by the absence of the transition zone) but it is way too high in MORR-CTL.

These findings are confirmed when looking at the temporal evolution of the radar reflectivity profiles simulated by MORR-CTL and THOM-CTL at a specific location. For qualitative comparisons with the RWP reflectivity, Fig. 11 shows examples of such cross sections close to the ARM SGP Central Facility. In both simulations, the leading convective line has a delay of about 1 h (Fig. 5). The subsequent stratiform region is slightly too short in MORR-CTL and slightly too long in THOM-CTL. Since a model cannot be expected to reproduce observations at one location, several vertical cross sections obtained at different positions (see crosses in Fig. 4e) are shown in Figs. S1 and S2 in the online supplemental material. While the different cross sections show some variability, a leading convective cell with trailing stratiform precipitation of comparable duration is always found. As expected, the properties of the convective cells (such as their duration or the highest altitude of the 50-dBZ level) are highly variable in space. Nevertheless, several features are found to be common for stratiform parts of most cross sections:

- Similarly to previous work on intense convective systems (Lang et al. 2011; Fan et al. 2017; Varble et al. 2014b), the ice reflectivity is largely overestimated by MORR-CTL in the stratiform part. Various explanations of this high bias have been found in literature: Lang et al. (2011) assumed that it was driven by wrong proportions of the different ice categories while Varble et al. (2014a) found that too strong simulated deep convective updraft produced too much condensate aloft, but also suggested that the lower-exponent parameter of the snow category in the Thompson et al. (2008) scheme (the snow mass is assumed to be proportional to $D^{1.9}$ as snow observations suggest, instead of D^3) could explain its better performances. This will be further explored in Part II in view of the comparisons of the simulated ice and graupel mixing ratios with the retrieved ice water contents from the ARM wind profiler.
- Likewise, the bright band reflectivity is largely overestimated in MORR-CTL whereas it appears too thin in THOM-CTL. Since both schemes use the same assumptions to compute the radar reflectivity of partially melted ice (G. Thompson 2018, personal communication) [i.e., the approach described in Blahak (2007)], this can only be explained by a different partitioning between the ice categories and/or by the different assumptions on the ice species (e.g., the mass–size relation used for snow) in each scheme. While other models can predict or diagnose the liquid fraction of melting hydrometeors (Ferrier 1994; Walko et al. 1995; Loftus et al. 2014; Planche et al. 2014; Xue et al. 2017), the computation of partially melted ice reflectivity is challenging and requires a large number of assumptions such as on the air-water-ice mixture. Therefore, it is not a surprise that WRF is not able to reproduce the melting layer reflectivity in the current case.
- As in Varble et al. (2014b), rain reflectivities in the stratiform part are overestimated by MORR-CTL while they are quite well reproduced by THOM-CTL.
- Regarding the TZ, a reflectivity minimum is observed above the melting level for MORR-CTL but neither of the simulations is able to reproduce the clear 1-h-long rain reflectivity weakening transition zone of the observations. Even though mesoscale simulations are able to produce a TZ in idealized frameworks (Morrison et al. 2012), it is well known that it is often challenging in real cases (Fan et al. 2017; Jensen et al. 2018) as a result of the complex interplay between 3D dynamics and ice properties.

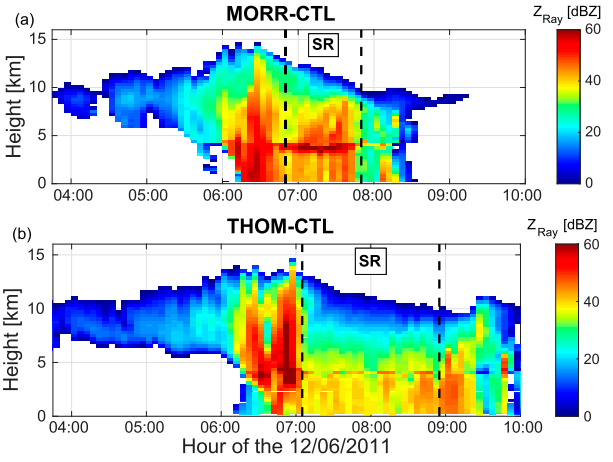

FIG. 11. Examples of time–height evolution of the Rayleigh radar reflectivity obtained with the (a) MORR-CTL and (b) THOM-CTL simulations at/close to the position of the SGP Central facility. Additional cross sections can be found in the supplemental material.

It is not realistic to make a point to point quantitative evaluation of the 3D dynamics of the simulated squall line, in particular within the convective region. However, 3D winds in squall lines are generally consistent in the along-line direction and qualitative comparisons at a single location can further confirm if the 3D structure of the squall line is sensible. 3D wind retrievals are performed over SGP using the multi-Doppler technique (Shapiro et al. 2009; Potvin et al. 2012) by combining the three nearby WSR-88D radars KVNX, KINX, and

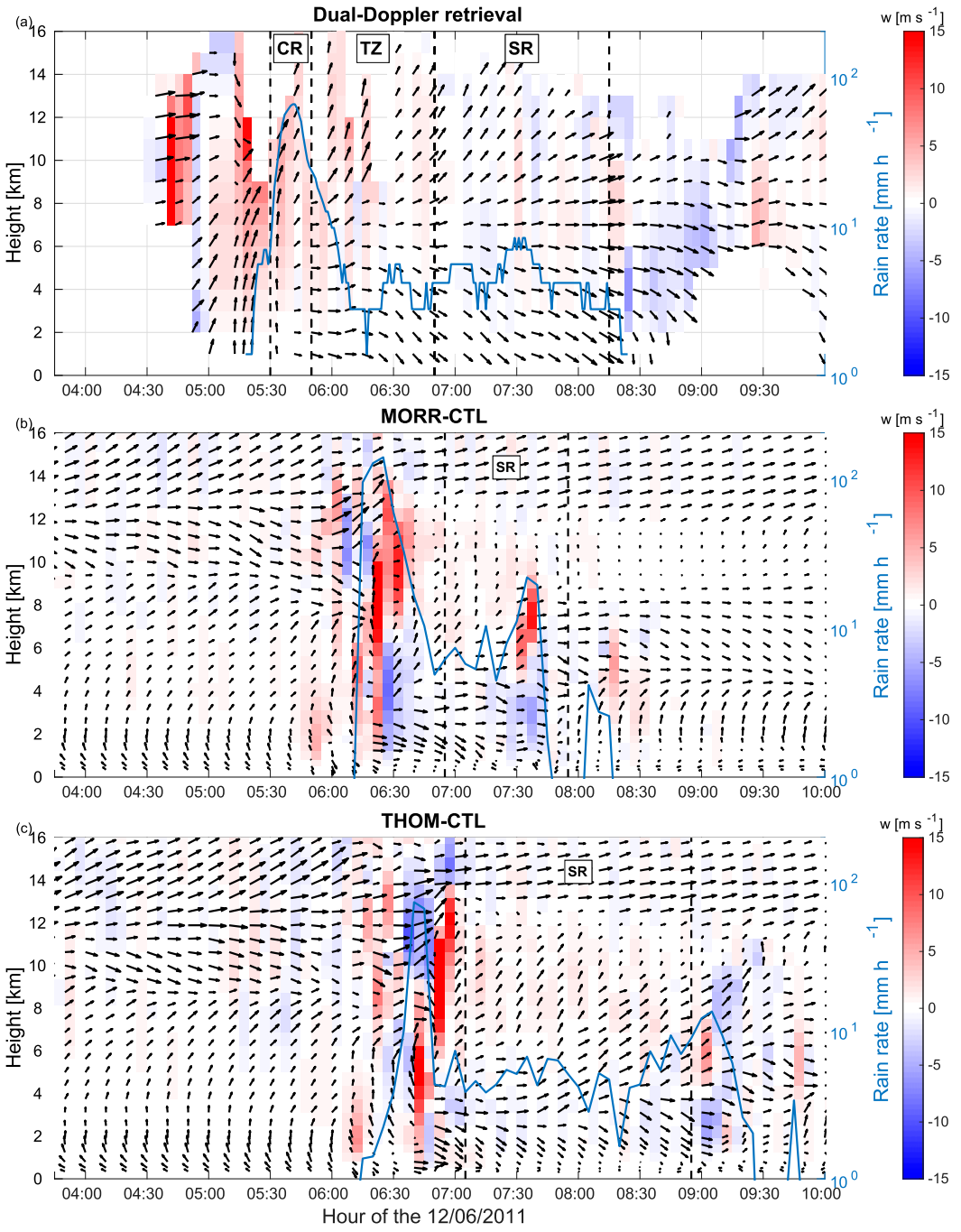

FIG. 12. (a) Horizontal (direction and intensity showed by black arrows orientation and length, respectively) and vertical (color shading) wind profiles retrieved and (b) simulated in MORR-CTL and (c) THOM-CTL at or close to the SGP site (positive values in red correspond to updraft). The corresponding rain rate at the ground (blue line and right *y* axis) helps to interpret the 3D winds with respect to the time evolution of the squall line.

KTLX. The results are compared in Fig. 12 with the simulated 3D wind profiles close to SGP (at the location where the reflectivity fields of Fig. 11 have been derived). Observations and simulations show the typical characteristics of squall-line dynamics (see e.g., Braun and Houze 1994).

- Strong wind shear is present ahead of the rain-rate peak at the ground (again with a 1 h delay in the simulation), with southerly winds at low level (2 km) gradually turning toward westerly winds at 10 km. In the model, however, the altitude of the shear layer

appears slightly too low (around 7 km instead of 9 km) and the intensity of the shear is overestimated because of too weak winds below 7 km.
- A lower-level rear inflow circulation is revealed by a larger eastward component of the winds close to the surface after the rain-rate peak.
- An upper-level weak ascent is associated with a front to rear circulation, as highlighted by the reduced eastward component of the winds after the rain-rate peak. One major difference is that the northward component of the wind in this zone is much larger in the observations than in the simulations.
- Observed and simulated vertical winds properties are similar after the rain peak with a weak mesoscale updraft and downdraft above and below 4 km, respectively. Note, however, that the error of the retrievals is of the order of 2 m s^{-1} (Potvin et al. 2012).

In summary, the comparison of observed and modeled reflectivity and dynamics shows that the WRF simulations are able to reproduce the structure and evolution of the squall line (i.e., a mature squall line with a leading convective line followed by widespread stratiform precipitation). One major difference is the inability of the model to reproduce the transition zone between these two regions, a known issue that is not addressed in this study. Focusing on the stratiform region, its duration and associated 3D winds are quite well reproduced while reflectivity comparisons confirm previous findings with a tendency to overestimation in the MORR-CTL simulation, in particular in the ice phase. Before assessing the microphysics properties of rain in the stratiform region, quantitative comparisons of the vertical wind and of the relative humidity will be performed in the following section.

c. *Statistical analysis of the dynamics and thermodynamics properties within the stratiform region*

The instrumentation available at the SGP site can be used to quantitatively compare the simulated dynamics and thermodynamics in the stratiform region. The vertical wind obtained from the DSD retrieval (Fig. 8d) and the relative humidity retrieved by the ARM Raman lidar are relevant in this context.

Comparison of model results with profiling observations are challenging because a model cannot be expected to reproduce exact system evolution in space and time, and the representativeness of a single event time–height is unknown. One solution is to compare statistically the observations at SGP to a large number of model columns over the whole simulated squall line. For this aim, 20 vertical cross sections (such as those in Fig. 11 and Figs. S1 and S2) are obtained from different positions within the squall line. From those cross sections, in order to mimic the properties of the observed SR in Figs. 5a and 8d, all the stratiform regions are detected as contiguous regions with the rain reflectivity at 2 km higher than 30 dBZ and the rain rate lower than 20 mm h^{-1}. Since the main objective of this study is not to understand why the simulations cannot reproduce the TZ, these columns are then combined disregarding their distance from the convective line. For any modeled parameter, this forms a distribution of more than 100 samples from which the median and the first and third quartiles can be computed. Note that this representation was chosen for its readability but another solution would be to compare the observed median profile to the ensemble of median profiles of the 20 modeled cross sections.

Following this procedure, Fig. 13 compares the profile of the vertical wind simulated with MORR-CTL (Fig. 13b) and THOM-CTL (Fig. 13c) to the profile of the retrieved vertical wind distribution (Fig. 13a) obtained from the data of Fig. 8d. Because it has a much higher temporal resolution than the cross sections obtained from the model, the unique cross section of the retrieved vertical wind at SGP has a slightly larger number of samples. With no surprise, the distribution of the retrieved vertical wind contains more extreme values since the sampling volume of the cloud radars is much smaller than the size of the model box. Nevertheless, the median and quartiles of the retrieved and modeled vertical wind profiles are in good agreement and confirm a weak downdraft over the whole rain layer (with vertical wind close to 0 m s^{-1} near the ground and as low as -0.5 m s^{-1} at 3-km height).

Because of this mesoscale downdraft, the stratiform part in squall lines is known to be particularly dry. This can be checked following the same procedure for the observed and modeled relative humidity (RH). In this case, standard measurements by radiosoundings do not bring much information on RH in the stratiform part of the squall line because they were launched at 0522 and 1728 UTC, that is, just before the rain onset and more than 8 h after the rain stopped, respectively. On the contrary, at the SGP site, Raman lidar observations continuously provide high-resolution retrievals of RH profiles (Turner et al. 2002; Flynn et al. 2016). The structure of the retrieved RH (Fig. 14) is sensible throughout the squall line, with, for example, values approaching 100% at 0500 UTC and 2 km where the presence of a cloud prevents any retrieval at higher altitudes because of the complete extinction of the lidar backscatter. Elsewhere, the signal-to-noise ratio is high enough to provide a spatially coherent RH up to about

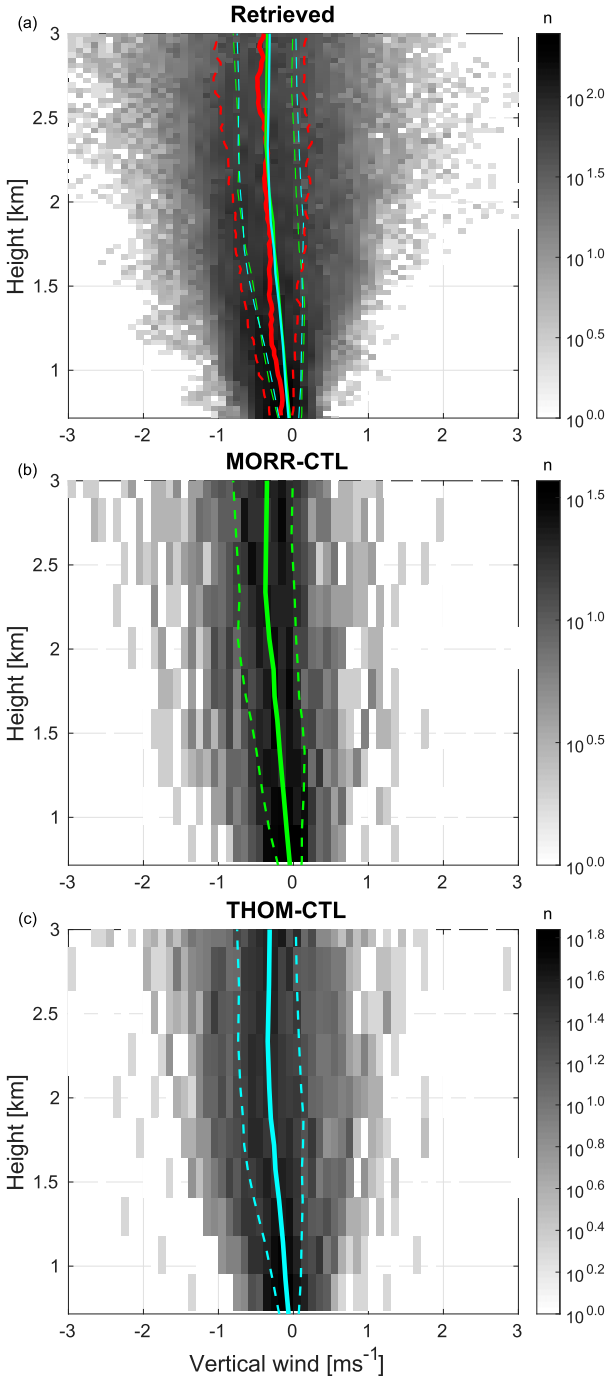

FIG. 13. (a) Profile of the probability density functions (PDFs) of the vertical wind in the SR retrieved in the framework of the DSD retrieval, (b) simulated in MORR-CTL, and (c) simulated in THOM-CTL, with the color scale indicating the number of samples *n*. The PDFs should not be directly compared because they correspond to different types of data (single vs 20 cross sections, different time and spatial resolutions). More comparable are the continuous and dashed lines that show the median and the first and third quartiles in red, green, and cyan for the retrieval, the MORR-CTL, and THOM-CTL simulation, respectively.

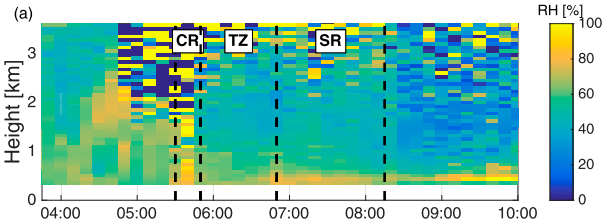

FIG. 14. Time–height evolution of the relative humidity over SGP as retrieved with the Raman lidar.

2.5 or 3 km, apart from the profile retrieved during the CR whose variability make it questionable. This retrieval is an official ARM value added product that has been widely used during the last couple of decades (Turner et al. 2016, and references therein). Errors in the RH retrieval of the order 10% are expected during daytime due to high solar background levels (Turner and Goldsmith 1999). However, rainy conditions are not ideal for lidar observations and it is preferable to verify the quality of these retrievals via comparisons with measurements at the surface and on top of a 60-m tower (Fig. 15). At the exception of the period of heavy rain where accurate RH measurements are not surprisingly challenging with any type of instrument, the Raman lidar retrievals at the lowest range gate (purple line) are in agreement with the tower measurements (yellow line) within about 10% of RH overall, and up to 20% in some parts of the TZ and the SR. This is confirmed by the comparisons of the retrieval and radio sounding measurements at 1 km (green line and black circles). Finally, the measurements taken at the three levels of the meteorological tower (ground, 25 and 60 m) show that RH increases toward the ground in the SR, a feature that the Raman lidar retrieval is able to reproduce. In summary, the retrieval suggests a consistently dry atmosphere during the TZ and the SR with values as low as 40% between 1 and 3 km MSL (Fig. 14).

Because the resolution of the Raman lidar retrieval is 10 min, only eight profiles are retrieved within the SR. Hence, their distribution is not very instructive and only their median is compared with the median modeled RH in Fig. 16 (the spread of the observations must be interpreted with caution because it is probably not representative). While retrieved and simulated profile agree on a minimum RH situated between 1.5- and 2-km height, the simulated RH is significantly overestimated by more than 10%, with a minimum RH of 55% at 1.5 km for MORR-CTL and 60% at 1.9 km for THOM-CTL.

d. Statistical analysis of the rain microphysics properties in the stratiform region

Following the methodology of the previous section, the profiles of the simulated rain mass mixing ratio q_r,

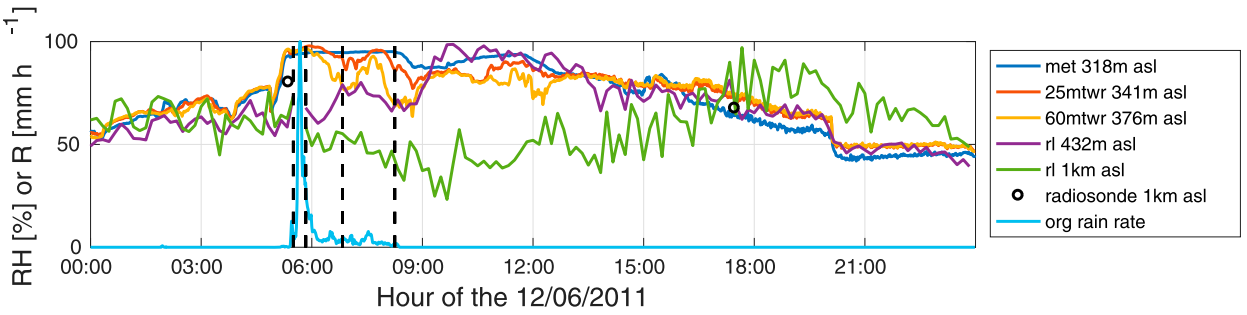

FIG. 15. Comparison of the Raman lidar RH retrieval at two levels (432 m, purple line, and 1 km, green line) with other observations available at the SGP site: at the surface (blue line), on the meteorological tower (25 m, orange line, and 60 m, yellow line), and at 1 km by radio soundings (black circles). The rain rate measured by the collocated optical rain gauge is shown for reference (cyan line).

mean volume diameter D_m, and concentration parameter N_0^* are statistically compared with the retrieved ones in Figs. 17–19, respectively. Note that it was decided to compare N_0^* because it was directly provided by the retrievals but a comparison could have been done equivalently on the number concentration N_r—usually employed in modeling studies—since these two parameters are directly related via the relationship $N_0^* = 4N_r/D_m$ for exponential distribution.

The median retrieved q_r profile shows a continuous decrease from 3 km down to the ground. This is consistent with active evaporation within this dry layer. This behavior is impressively well reproduced by both microphysics schemes with a slight shift of the whole MORR-CTL profile toward smaller values. Despite this very good agreement in q_r, the D_m and N_0^* profiles are significantly different from the observations in both schemes.

The MORR-CTL simulation shows a strong increase of D_m toward the ground that is not seen in the observations as it was already found by Morrison et al. (2012) and Varble et al. (2014b). As noticed by Varble et al. (2014b), D_m largely exceeds the value of the equilibrium DSD (2 mm, see section 3c) as it approaches the ground. A novelty of the current work is the evidence that this is compensated by an excessive decrease of N_0^* Several factors can explain such a behavior: uncontrolled size sorting (Wacker and Seifert 2001; Milbrandt and McTaggart-Cowan 2010), an inadequate parameterization of drop breakup and self-collection, or excessive evaporation. While higher evaporation is a candidate to explain the anomalous D_m and N_0^* profiles, it is not compatible with the air being less dry in MORR-CTL than in the observations. This will be further investigated in the companion paper via sensitivity studies.

While the spread of D_m and N_0^* in the THOM-CTL simulation is larger than in the observations with more numerous extreme values, the averaged vertical variation is comparably weak. However, this may be the result of an artificial upper limit on D_m at 2.8 mm, which is evident in Fig. 18c. In fact, this leads to a bimodal distribution of D_m values and, despite an average close to the observations, a significant number of unrealistic D_m profiles are present. As it will be further discussed in the companion paper (Part II), such limit is indeed used in the Thompson scheme in order to control the size sorting of raindrops.

5. Conclusions

This paper investigates how well the observed microphysics characterization of rain in the stratiform part of a squall line can be reproduced by the WRF Model with two bulk microphysics schemes. A squall line observed on 12 June 2011 over Oklahoma, for which unique dual-frequency cloud radar observations were available for the entire duration of the rain event, is used as a case study. Using the Thompson et al. (2008) and Morrison et al. (2009) microphysics schemes, the model

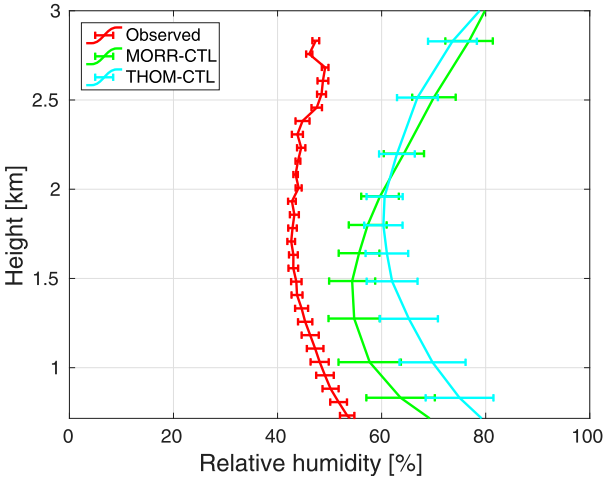

FIG. 16. Profile of the median RH retrieved by the Raman lidar (red), simulated in MORR-CTL (green), and simulated in THOM-CTL (cyan). The error bars show the spread between the first and third quartiles.

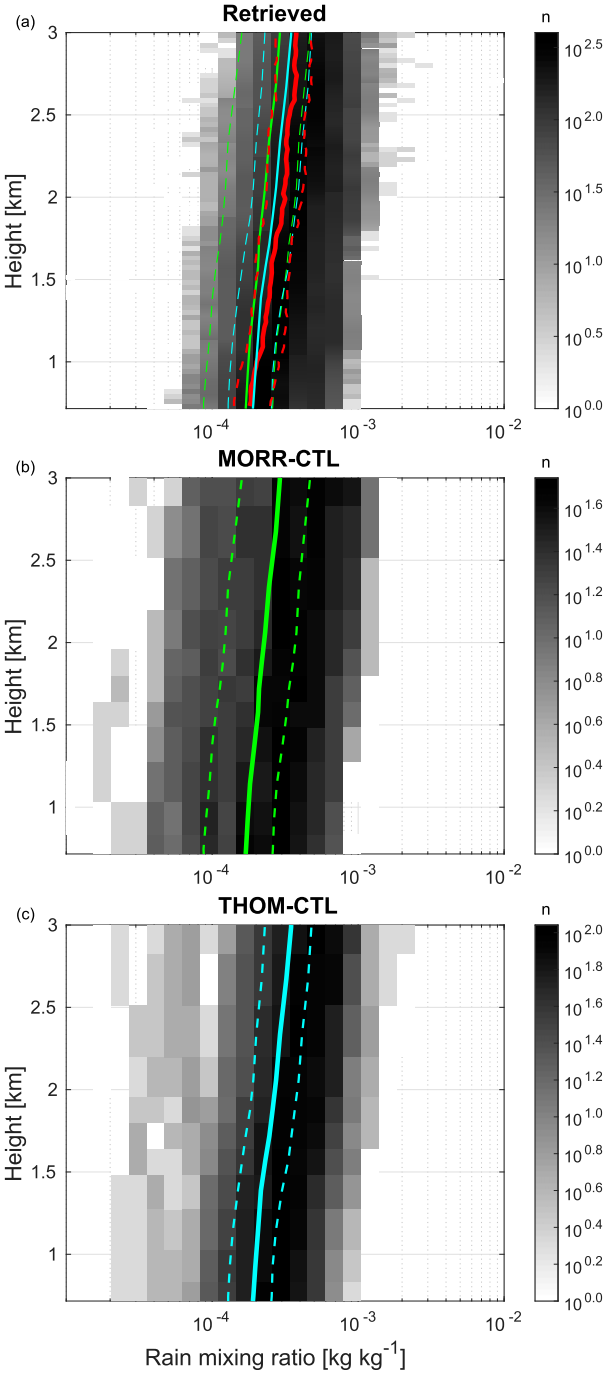

FIG. 17. As in Fig. 13, but for q_r.

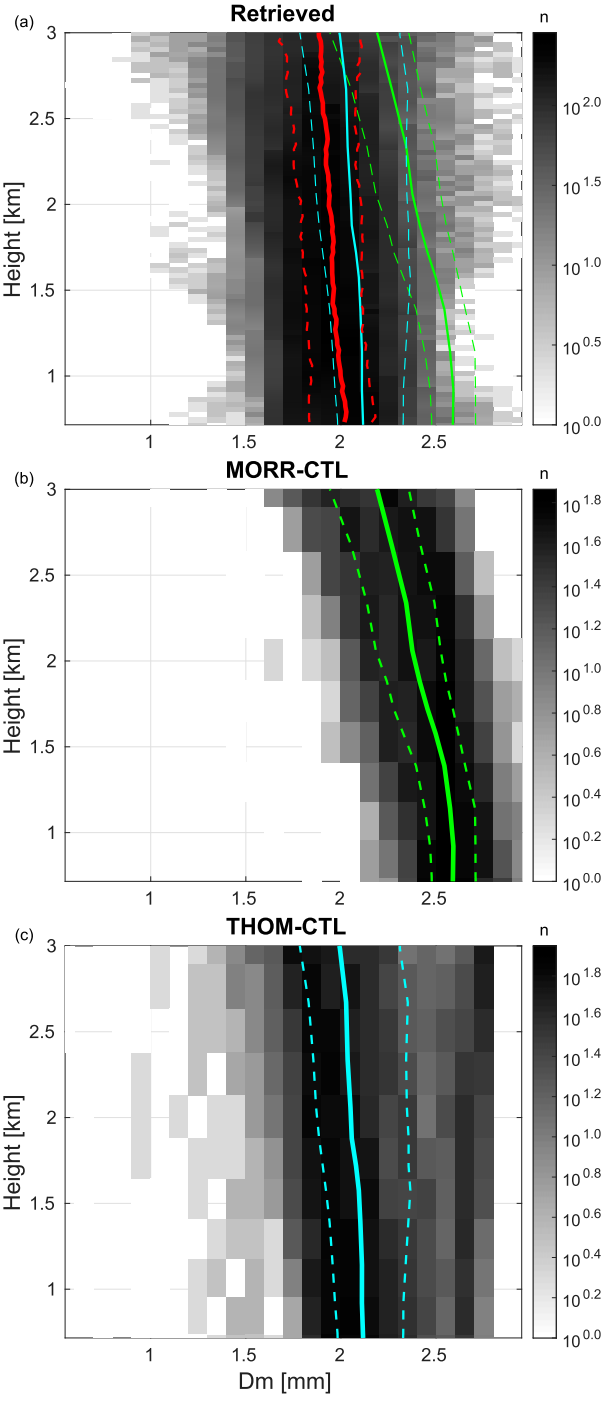

FIG. 18. As in Fig. 13, but for D_m.

is able to reproduce the extent and evolution of the squall line with a leading convective line and a trailing wide stratiform region. However, both microphysics schemes fail to reproduce the 1-h low-reflectivity transition region observed by radars. While this comparison is primarily qualitative, the reflectivity is significantly overestimated when using the Morrison et al. (2009) microphysics scheme, confirming previous works on squall-line simulations.

Such disagreement is further investigated by exploiting a recently developed retrieval technique applied to K_a- and W-band vertically pointing cloud radar observations that provides the vertical evolution of the DSDs.

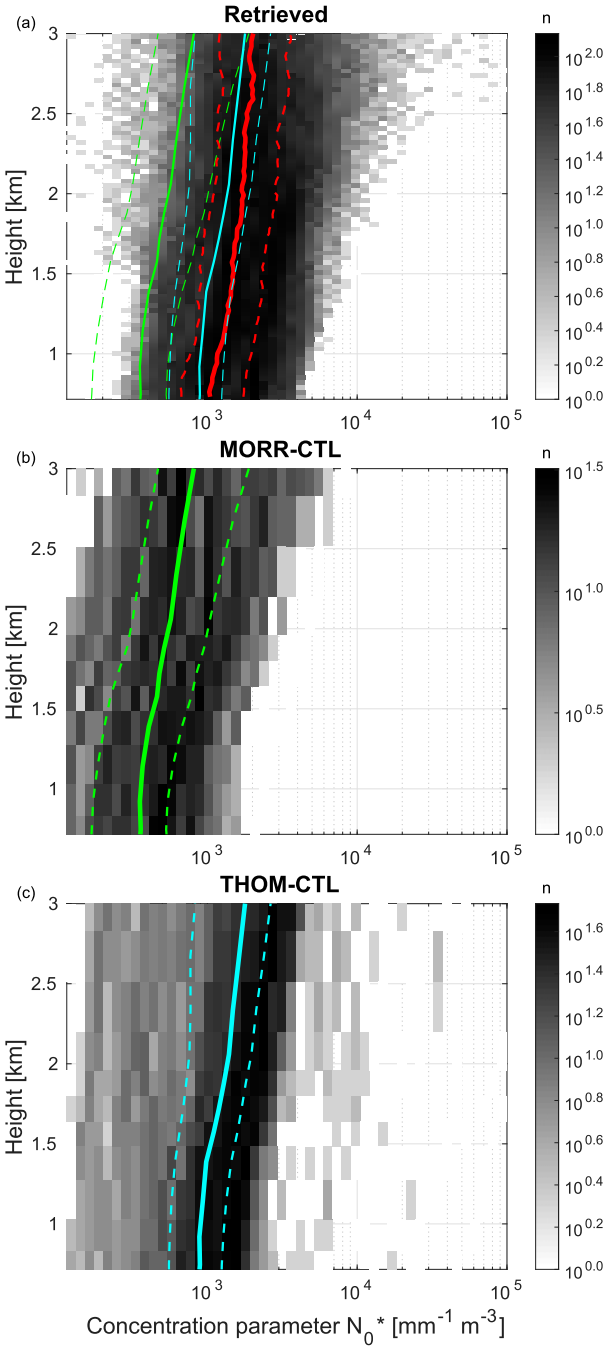

FIG. 19. As in Fig. 13, but for N_0^*.

The results of such retrievals are compared to more conventional retrievals from a nearby polarimetric radar. This comparison demonstrates the complementarity of these two types of retrievals, with the first one covering extended areas but with less accuracy and the second one providing a much more detailed description of the DSD vertical and temporal variations in the transition and stratiform regions, but only for a precipitation column. The dual-frequency technique is, however, limited to light and moderate rainfall as cloud radars suffer from strong attenuation in heavy rain.

In the stratiform region, both simulations are able to reproduce the observed mesoscale downdraft and the associated significative subsaturated air mass below the melting level. However, ancillary retrieval of relative humidity with a Raman lidar (RH as low as 44%) shows that it is slightly overestimated in the simulations [55% and 60% for Morrison et al. (2009) and Thompson et al. (2008) schemes, respectively]. The rain microphysics profiles simulated by WRF are then compared to the detailed description of DSD variability in this region. While the simulated rain mixing ratio is in good agreement with observations and shows a continuous decrease that can be explained by evaporation in the subsaturated air, the profiles of mean volume diameter D_m and concentration parameter N_0^* are not well reproduced. The Morrison et al. (2009) scheme leads to an excessive increase of D_m toward the ground that is compensated for by an excessive decrease of N_0^*. Conversely, the Thompson et al. (2008) scheme leads to average profiles of D_m and N_0^* closer to the observations but with a significantly different D_m distribution. In both case, these discrepancies might be explained by the inadequate representation of the active rain microphysics processes (i.e., drop breakup, self-collection, evaporation, or size sorting under sedimentation). They can also be partly driven by differences in the rain DSD just below the bright band, which can be related to possible model deficiencies in the ice phase. This will be further investigated in the companion paper via sensitivity studies.

Acknowledgments. We thank the associate editor Hugh Morrisson, Alain Protat, and two other anonymous reviewers for their interesting comments that greatly helped to improve the manuscript. This work was funded by the project "Evaluation de la Modélisation microphysique des Précipitations à l'aide d'Observations Radars Multi-fréquences (EMPORiuM)" funded by the French CNRS-INSU LEFE-IMAGO programme. This research used the SPECTRE and ALICE High Performance Computing Facilities at the University of Leicester. The WRF calculations have been done on French computer facilities of the Institut du Développement des ressources en Informatique Scientifique (IDRIS) CNRS at Orsay, the Centre Informatique National de l'Enseignement Supérieur (CINES) at Montpellier under the project 940180 and the Centre Régional de Ressources Informatiques (CRRI) at Clermont-Ferrand. The lead author was supported in part by the project "Calibration and validation studies over the North Atlantic and U.K. for Global Precipitation Mission" funded by the U.K. NERC (NE/L007169/1)

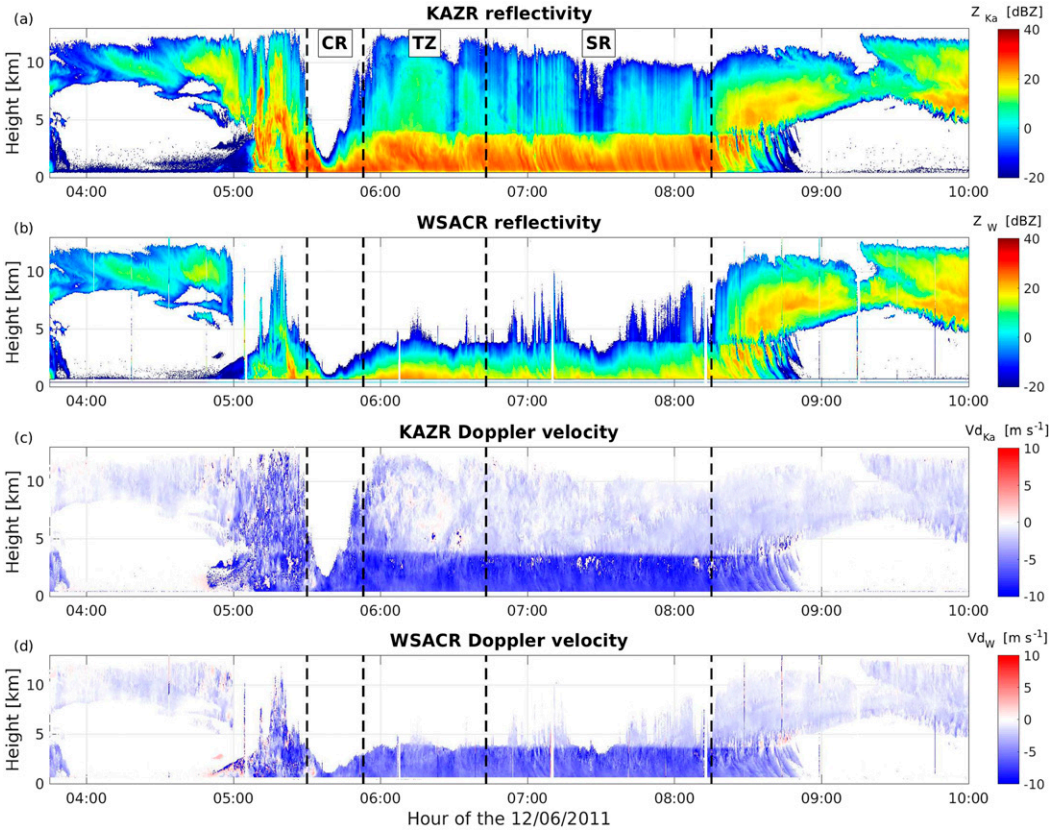

FIG. A1. Time–height evolution of the ARM cloud radars collocated with the ARM radar wind profiler (cf. Fig. 5): (a) K_a-band reflectivity, (b) W-band reflectivity, (c) K_a-band Doppler velocity, and (d) W-band Doppler velocity. Upward velocity is defined as positive.

and by the Atmospheric System Research Project DE-SC0017967. Data were obtained from the U.S. DOE ARM Climate Research Facility www.archive.arm.gov and from the U.S. NOAA/NSSL MRMS system available at http://mrms.ou.edu. KVNX, KINX, and KTLX data were obtained from the National Oceanic and Atmospheric Administration via AmazonWeb Services (https://aws.amazon.com/noaa-bigdata/nexrad/). Their data were ingested, edited, and analyzed using the Py-ART (http://arm-doe.github.io/pyart/), CSU_RadarTools (https://github.com/CSU-Radarmet/CSU_RadarTools), and MultiDop (https://github.com/nasa/MultiDop) open-source packages.

APPENDIX

General Principle of the Multifrequency Radar Retrieval Technique

a. *Influence of the radar frequency on observed radar moments*

Cloud radars observables (Figs. A1a,b) provide synergistic and complementary information to more conventional precipitation radars. Because of the frequency dependence of hydrometeor backscattering cross sections, larger frequencies—$\upsilon_{RWP}(\approx 1\,GHz) < \upsilon_{K_a}(35\,GHz) < \upsilon_W(94\,GHz)$—lead to greater sensitivities and thus can detect smaller hydrometeors (Lhermitte 1990); for example, compare the cloud radar with RWP reflectivities (Fig. 5a) corresponding to the ice crystals forming the ice deck between 8 and 12 km before 0500 UTC. However, attenuation by hydrometeors generally increases with frequency leading to full extinction of the radar signal at low levels in case of heavy rain at the highest frequencies (e.g., at 1 km and 300 m for K_a- and W-band, respectively, during the most intense rainfall period at 0545 UTC). Additionally, at larger frequencies, the backscattering cross section of large hydrometeors generally decreases (the so-called non-Rayleigh effects; Tridon et al. 2013a), which also explains why $Z_W < Z_{K_a} < Z_{RWP}$ at short range (see e.g., at around 0600 UTC and 1-km height). Finally, the Doppler velocity (Figs. A1c,d) highlights the contrast between ice crystals and raindrops fall velocities in the SR, and some rapidly alternating updrafts and

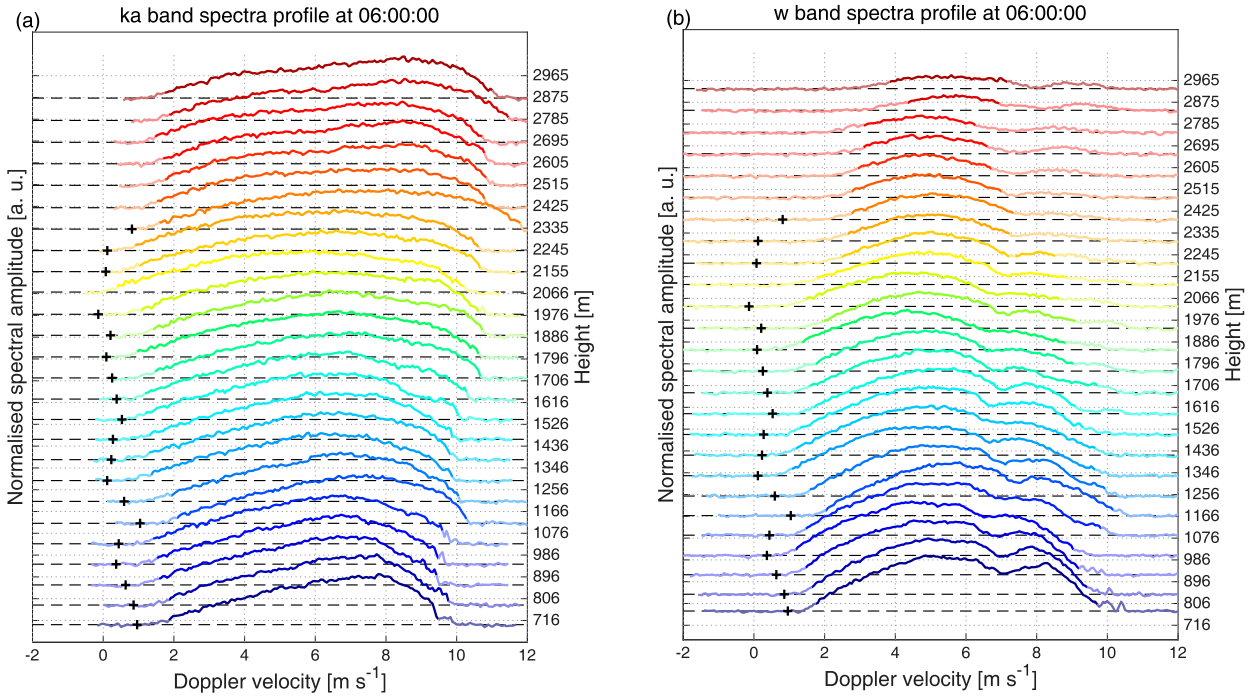

FIG. A2. Doppler spectra profile observed within the transition zone at 0600 UTC by (a) the K_a- and (b) the W-band radars, respectively. The retrieved vertical wind (positive downward) is indicated at each level by the black crosses.

downdrafts in the CR [mainly visible in Fig. 5b because of the smaller Nyquist velocity used by cloud radars that leads to Doppler velocity aliasing (Tridon et al. 2011)]. Another consequence of the non-Rayleigh effects is that the Doppler velocity in rain is smaller at W band (Fig. A1d) because the reflectivity is dominated by smaller drops that fall at lower velocities.

By combining the observations from the different radars, the peculiarities observed at each different frequency become an advantage and allow to quantitatively retrieve the hydrometeors properties with an accuracy that would not be possible with a single radar. In particular, for the squall-line case study presented in this work, the method of Tridon and Battaglia (2015) and Tridon et al. (2017a) enables retrieval of DSD profiles from observations of K_a- and W-band Doppler spectra.

b. *Effect on radar Doppler spectra and DSD retrieval*

Radar Doppler spectra represent the spectral reflectivity per bin of Doppler velocity. Thanks to the relationship between drop fall speeds and sizes, the shape of Doppler spectra obtained in a vertically pointing mode is intimately related to the particle size distribution, with the mean air motion displacing all hydrometeors equally and shifting the whole spectra along the Doppler velocity axis. On the contrary, depending on the position within the radar volume, the apparent velocity of similar sized hydrometeors can be modified differently by air turbulence, wind shear and/or crosswind, all effects adding up in the so-called spectral broadening. For these reasons, the retrieval of DSD from Doppler spectra relies on accurate estimates of spectral broadening and vertical air motion that are not realistically possible with a single-frequency Doppler spectrum (Atlas et al. 1973).

At millimeter wavelength, scattering by raindrops depends on the frequency of the transmitted wave according to the Mie theory (Lhermitte 1990): the backscattering power oscillates with consecutive maxima and minima with increasing drop size and these oscillations modulate the Doppler spectrum with the possibility of producing multimodal spectra at W band, with a characteristic Mie notch corresponding to drops of 1.67-mm diameter. This is demonstrated in Figs. A2 and A3, which show examples of Doppler spectra profiles observed by ARM K_a- and W-band radars during the transition zone (at 0600 UTC) and the stratiform period (at 0745 UTC), respectively. Differences between the two radar frequencies are evident with Mie notches clearly visible in the W-band Doppler spectra between 6 and 8 $m\,s^{-1}$. Such differences are exploited to deduce the vertical air motion (whose retrieved magnitude are indicated by black crosses) and the spectral broadening; then the spectral reflectivity in each Doppler velocity bin is converted into a drop

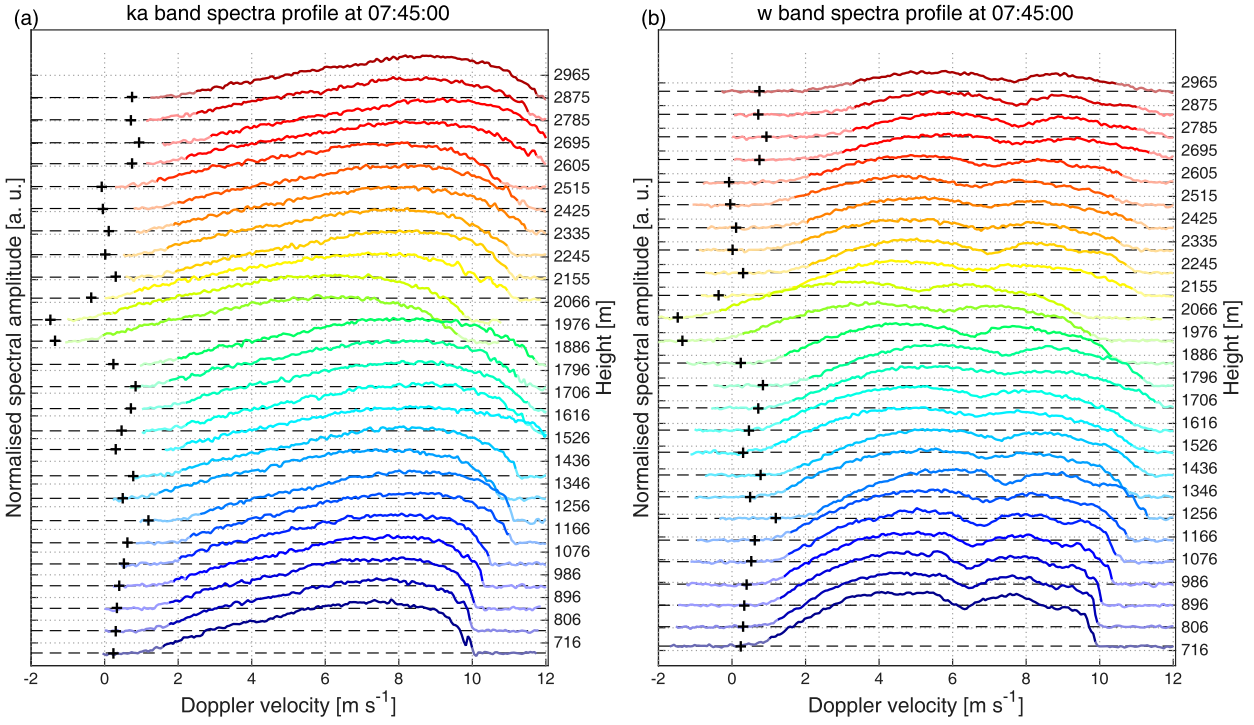

FIG. A3. As in Fig. A2, but for the stratiform period at 0745 UTC.

concentration of the corresponding diameter. Another noticeable feature in Figs. A2 and A3 is the reduction of the dynamic range of the Doppler spectra with height, especially at W band. This is due to a lower signal-to-noise ratio at longer ranges because of the attenuation produced by rain and air along the path. Tangible rain attenuation is actually necessary to calibrate the spectral reflectivities and correct for possible wet radome attenuation (Tridon et al. 2017a). However, in case of heavy rain and strong attenuation, the W-band spectra have very low signal-to-noise ratio in the majority of the Doppler velocity bins so that the retrieval becomes inapplicable, as it is the case on the 0600 UTC profile above 2.4 km AGL (Fig. A2b).

Comparing the profiles in Figs. A2 and A3, the Doppler spectra at 0745 UTC are much wider than at 0600 UTC—in Fig. A3b, a secondary Mie notch is even somewhat visible at 9 m s^{-1} below 1 km (Giangrande et al. 2012)—indicating that larger drops are present in the stratiform period. This is confirmed in the corresponding retrieved DSD profiles (Fig. A4): while the DSD at 0600 UTC can be practically approximated by a

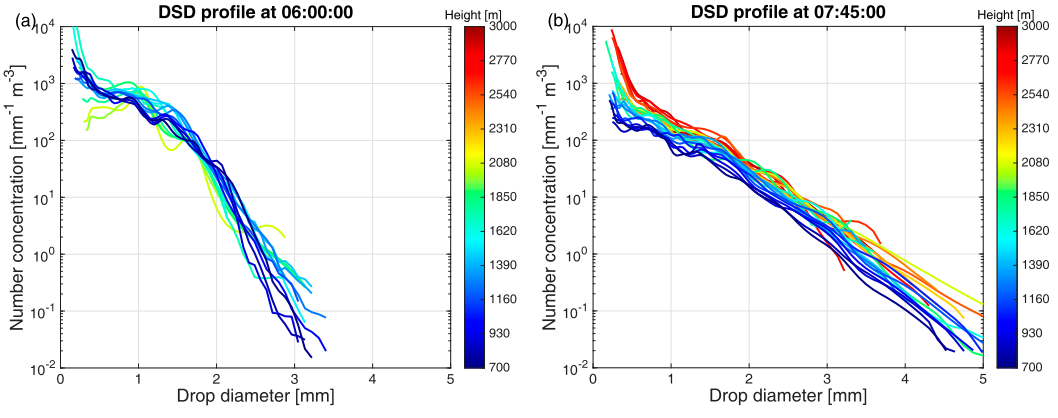

FIG. A4. Vertical evolution of retrieved DSD profiles at (a) 0600 and (b) 0745 UTC. Each color corresponds to a different height as indicated in the color bar.

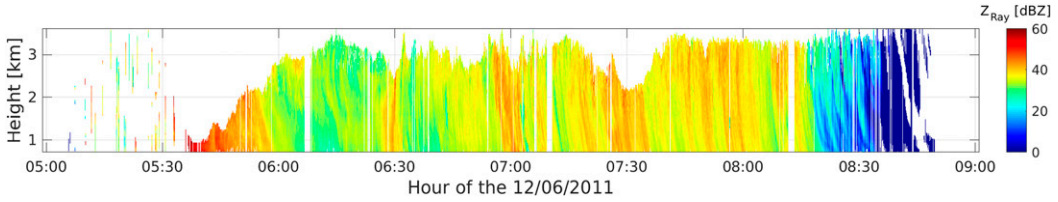

FIG. A5. Rayleigh reflectivity forward modeled from the retrieved DSDs.

piecewise linear function with a more rapid decrease in the concentration of drops larger than 1.8 mm, the DSD at 0745 UTC is almost exponential with drops as large as 5 mm. The vertical variation of the DSD corresponding to radar profiles averaged over ≈2–4 s is challenging to interpret because precipitation is mainly advected during such very short time scale. This issue can be mitigated by averaging the retrieved DSD profiles over a sufficiently long period (Tridon et al. 2017b). Both transition and stratiform periods are long enough (60 and 85 min, respectively) to provide meaningful vertical variation of the DSD that are further exploited in this paper.

c. Validation of the DSD retrieval

An indirect validation of the retrieval is possible via the comparison of the reflectivity observed by the RWP with the Rayleigh reflectivity computed (or forward-modeled) from the retrieved DSDs (Fig. A5). Because of non-Rayleigh effects and heavy rain attenuation, the reflectivity measured by K_a- and W-band cloud radars is not simply proportional to the sixth moment of the DSD, and their reflectivity fields (Figs. A1a,b, respectively) differ greatly from the RWP one (Fig. 5a). Nevertheless and despite the large mismatch in their beamwidths, the RWP reflectivity details are very well reproduced from the DSD retrieval (Fig. A5). For a more quantitative comparison, the forward-modeled reflectivity is averaged to match the resolution of the RWP reflectivity and the probability density function of their difference is shown for each range gate in Fig. A6. The difference in the radar sampling volumes is large and increases with height, which explains why the reflectivity difference spread over a significant interval (−3 to +3 dB), which also slightly increases with range. On the contrary, the mean difference is lower than 0.5 dB over the whole profile (up to 3 km), which demonstrates the good accuracy of the retrieval.

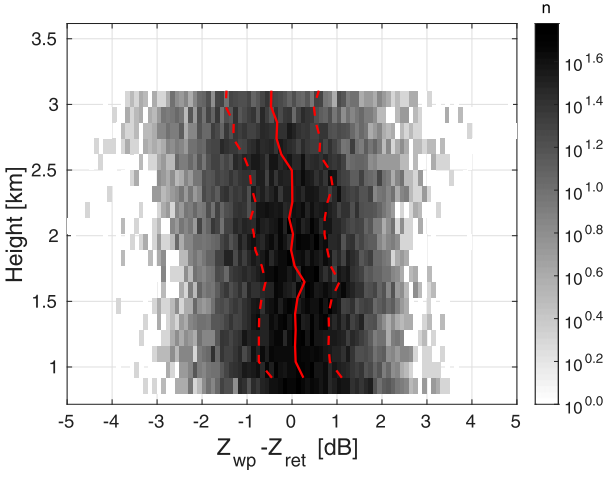

FIG. A6. Profile of the probability density functions of the difference between the reflectivity observed by the RWP and forward modeled from the DSD retrieval. The continuous and dashed red lines show the mean and the first and third quartiles.

REFERENCES

Atlas, D., R. C. Srivastava, and R. S. Sekhon, 1973: Doppler radar characteristics of precipitation at vertical incidence. *Rev. Geophys.*, **11**, 1–35, https://doi.org/10.1029/RG011i001p00001.

Barthes, L., and C. Mallet, 2013: Vertical evolution of raindrop size distribution: Impact on the shape of the DSD. *Atmos. Res.*, **119**, 13–22, https://doi.org/10.1016/j.atmosres.2011.07.011.

Biggerstaff, M. I., and R. A. Houze Jr., 1991: Kinematic and precipitation structure of the 10–11 June 1985 squall line. *Mon. Wea. Rev.*, **119**, 3034–3064, https://doi.org/10.1175/1520-0493(1991)119<3034:KAPSOT>2.0.CO;2.

——, and ——, 1993: Kinematics and microphysics of the transition zone of the 10–11 June 1985 squall line. *J. Atmos. Sci.*, **50**, 3091–3110, https://doi.org/10.1175/1520-0469(1993)050<3091:KAMOTT>2.0.CO;2.

Blahak, U., 2007: RADAR_MIE_LM and RADAR_MIELIB—Calculation of radar reflectivity from model output. Internal Rep., Institute for Meteorology and Climate Research, University of Karlsruhe, Karlsruhe, Germany, 150 pp.

Braun, S. A., and R. A. Houze Jr., 1994: The transition zone and secondary maximum of radar reflectivity behind a midlatitude squall line: Results retrieved from Doppler radar data. *J. Atmos. Sci.*, **51**, 2733–2755, https://doi.org/10.1175/1520-0469(1994)051<2733:TTZASM>2.0.CO;2.

——, ——, and M.-J. Yang, 1996: Comments on "The impact of the ice phase and radiation on a midlatitude squall line system." *J. Atmos. Sci.*, **53**, 1343–1351, https://doi.org/10.1175/1520-0469(1996)053<1343:COIOTI>2.0.CO;2.

Bringi, V. N., C. R. Williams, M. Thurai, and P. T. May, 2009: Using dual-polarized radar and dual-frequency profiler for DSD characterization: A case study from Darwin, Australia. *J. Atmos. Oceanic Technol.*, **26**, 2107–2122, https://doi.org/10.1175/2009JTECHA1258.1.

——, L. Tolstoy, M. Thurai, and W. A. Petersen, 2015: Estimation of spatial correlation of drop size distribution parameters and rain rate using NASA's S-band polarimetric radar and 2D video disdrometer network: Two case studies from MC3E. *J. Hydrometeor.*, **16**, 1207–1221, https://doi.org/10.1175/JHM-D-14-0204.1.

Bryan, G. H., and H. Morrison, 2012: Sensitivity of a simulated squall line to horizontal resolution and parameterization of microphysics. *Mon. Wea. Rev.*, **140**, 202–225, https://doi.org/10.1175/MWR-D-11-00046.1.

Chen, F., and J. Dudhia, 2001: Coupling an advanced land surface–hydrology model with the Penn State–NCAR MM5 modeling system. Part I: Model implementation and sensitivity. *Mon. Wea. Rev.*, **129**, 569–585, https://doi.org/10.1175/1520-0493(2001)129<0569:CAALSH>2.0.CO;2.

Cifelli, R., C. R. Williams, D. K. Rajopadhyaya, S. K. Avery, K. S. Gage, and P. T. May, 2000: Drop-size distribution characteristics in tropical mesoscale convective systems. *J. Appl. Meteor.*, **39**, 760–777, https://doi.org/10.1175/1520-0450(2000)039<0760:DSDCIT>2.0.CO;2.

Dawson, D. T., II, M. Xue, J. A. Milbrandt, and M. K. Yau, 2010: Comparison of evaporation and cold pool development between single-moment and multimoment bulk microphysics schemes in idealized simulations of tornadic thunderstorms. *Mon. Wea. Rev.*, **138**, 1152–1171, https://doi.org/10.1175/2009MWR2956.1.

Dee, D. P., and Coauthors, 2011: The ERA-Interim reanalysis: Configuration and performance of the data assimilation system. *Quart. J. Roy. Meteor. Soc.*, **137**, 553–597, https://doi.org/10.1002/qj.828.

Dudhia, J., 1989: Numerical study of convection observed during the winter monsoon experiment using a mesoscale two-dimensional model. *J. Atmos. Sci.*, **46**, 3077–3107, https://doi.org/10.1175/1520-0469(1989)046<3077:NSOCOD>2.0.CO;2.

Fan, J., and Coauthors, 2017: Cloud-resolving model intercomparison of an MC3E squall line case: Part I—Convective updrafts. *J. Geophys. Res. Atmos.*, **122**, 9351–9378, https://doi.org/10.1002/2017JD026622.

Feingold, G., R. Walko, B. Stevens, and W. Cotton, 1998: Simulations of marine stratocumulus using a new microphysical parameterization scheme. *Atmos. Res.*, **47–48**, 505–528, https://doi.org/10.1016/S0169-8095(98)00058-1.

Ferrier, B., 1994: A double-moment multiple-phase four-class bulk ice scheme. Part I: Description. *J. Atmos. Sci.*, **51**, 249–280, https://doi.org/10.1175/1520-0469(1994)051<0249:ADMMPF>2.0.CO;2.

Flynn, C., H. Sivaraman, J. Michelsen, R. Goldsmith, R. Bambha, and R. Newsom, 2016: Raman Lidar Mixing Ratio (RLPROFMR2NEWS10M) (12 June 2011). Southern Great Plains (SGP) Central Facility, Lamont, OK (C1), Atmospheric Radiation Measurement (ARM) Climate Research Facility, Oak Ridge, TN, accessed 27 January 2012, https://doi.org/10.5439/1415137.

Giangrande, S. E., E. P. Luke, and P. Kollias, 2012: Characterization of vertical velocity and drop size distribution parameters in widespread precipitation at ARM facilities. *J. Appl. Meteor. Climatol.*, **51**, 380–391, https://doi.org/10.1175/JAMC-D-10-05000.1.

Grecu, M., W. S. Olson, S. J. Munchak, S. Ringerud, L. Liao, Z. Haddad, B. L. Kelley, and S. F. McLaughlin, 2016: The GPM combined algorithm. *J. Atmos. Oceanic Technol.*, **33**, 2225–2245, https://doi.org/10.1175/JTECH-D-16-0019.1.

Hong, S.-Y., Y. Noh, and J. Dudhia, 2006: A new vertical diffusion package with an explicit treatment of entrainment processes. *Mon. Wea. Rev.*, **134**, 2318–2341, https://doi.org/10.1175/MWR3199.1.

Houze, R. A., 1993: *Cloud Dynamics*. Academic Press, 573 pp.

Hu, Z., and R. Srivastava, 1995: Evolution of raindrop-size distribution by coalescence, breakup and evaporation: Theory and observation. *J. Atmos. Sci.*, **52**, 1761–1783, https://doi.org/10.1175/1520-0469(1995)052<1761:EORSDB>2.0.CO;2.

Igel, A. L., M. R. Igel, and S. C. van den Heever, 2015: Make it a double? Sobering results from simulations using single-moment microphysics schemes. *J. Atmos. Sci.*, **72**, 910–925, https://doi.org/10.1175/JAS-D-14-0107.1.

Jensen, A. A., J. Y. Harrington, and H. Morrison, 2018: Microphysical characteristics of squall-line stratiform precipitation and transition zones simulated using an ice particle property-evolving model. *Mon. Wea. Rev.*, **146**, 723–743, https://doi.org/10.1175/MWR-D-17-0215.1.

Jensen, M. P., and Coauthors, 2016: The Midlatitude Continental Convective Clouds Experiment (MC3E). *Bull. Amer. Meteor. Soc.*, **97**, 1667–1686, https://doi.org/10.1175/BAMS-D-14-00228.1.

Jiménez, P. A., J. Dudhia, J. F. González-Rouco, J. Navarro, J. P. Montávez, and E. García-Bustamante, 2012: A revised scheme for the WRF surface layer formulation. *Mon. Wea. Rev.*, **140**, 898–918, https://doi.org/10.1175/MWR-D-11-00056.1.

Kessler, E., 1969: *On the Distribution and Continuity of Water Substance in Atmospheric Circulations. Meteor. Monogr.*, No. 32, Amer. Meteor. Soc., 84 pp.

Kirstetter, P.-E., J. J. Gourley, Y. Hong, J. Zhang, S. Moazamigoodarzi, C. Langston, and A. Arthur, 2015: Probabilistic precipitation rate estimates with ground-based radar networks. *Water Resour. Res.*, **51**, 1422–1442, https://doi.org/10.1002/2014WR015672.

Koenig, L. R., and F. W. Murray, 1976: Ice-bearing cumulus cloud evolution: Numerical simulation and general comparison against observations. *J. Appl. Meteor.*, **15**, 747–762, https://doi.org/10.1175/1520-0450(1976)015<0747:IBCCEN>2.0.CO;2.

Kollias, P., B. Albrecht, and F. Marks, 2002: Why Mie? Accurate observations of vertical air velocities and raindrops using a cloud radar. *Bull. Amer. Meteor. Soc.*, **83**, 1471–1483, https://doi.org/10.1175/BAMS-83-10-1471.

Lang, S. E., W.-K. Tao, X. Zeng, and Y. Li, 2011: Reducing the biases in simulated radar reflectivities from a bulk microphysics scheme: Tropical convective systems. *J. Atmos. Sci.*, **68**, 2306–2320, https://doi.org/10.1175/JAS-D-10-05000.1.

Lhermitte, R., 1990: Attenuation and scattering of millimeter wavelength radiation by clouds and precipitation. *J. Atmos. Oceanic Technol.*, **7**, 464–479, https://doi.org/10.1175/1520-0426(1990)007<0464:AASOMW>2.0.CO;2.

Loftus, A. M., W. R. Cotton, and G. G. Carrió, 2014: A triple-moment hail bulk microphysics scheme. Part I: Description and initial evaluation. *Atmos. Res.*, **149**, 35–57, https://doi.org/10.1016/j.atmosres.2014.05.013.

Maki, M., T. D. Keenan, Y. Sasaki, and K. Nakamura, 2001: Characteristics of the raindrop size distribution in tropical continental squall lines observed in Darwin, Australia. *J. Appl. Meteor.*, **40**, 1393–1412, https://doi.org/10.1175/1520-0450(2001)040<1393:COTRSD>2.0.CO;2.

Mason, S. L., J. C. Chiu, R. J. Hogan, and L. Tian, 2017: Improved rain rate and drop size retrievals from airborne Doppler radar. *Atmos. Chem. Phys.*, **17**, 11 567–11 589, https://doi.org/10.5194/acp-17-11567-2017.

Mather, J. H., and J. W. Voyles, 2013: The ARM Climate Research Facility: A review of structure and capabilities. *Bull. Amer. Meteor. Soc.*, **94**, 377–392, https://doi.org/10.1175/BAMS-D-11-00218.1.

Matthews, A., B. Isom, D. Nelson, I. Lindenmaier, J. Hardin, K. Johnson, and N. Bharadwaj, 2005: W-Band (95 GHz) ARM Cloud Radar (WACR) (12 June 2011). Southern Great Plains (SGP) Central Facility, Lamont, OK (C1), Atmospheric Radiation Measurement (ARM) Climate Research Facility, Oak Ridge, TN, accessed 13 June 2013, https://doi.org/10.5439/1025317.

——, ——, ——, ——, ——, ——, and ——, 2011: Ka ARM Zenith Radar (KAZRGE) (12 June 2011). Southern Great Plains (SGP) Central Facility, Lamont, OK (C1), Atmospheric Radiation Measurement (ARM) Climate Research Facility, Oak Ridge, TN, accessed 27 January 2012, https://doi.org/10.5439/1025214.

McFarquhar, G. M., 2004: A new representation of collision-induced breakup of raindrops and its implications for the shapes of raindrop size distributions. *J. Atmos. Sci.*, **61**, 777–794, https://doi.org/10.1175/1520-0469(2004)061<0777:ANROCB>2.0.CO;2.

Milbrandt, J. A., and R. McTaggart-Cowan, 2010: Sedimentation-induced errors in bulk microphysics schemes. *J. Atmos. Sci.*, **67**, 3931–3948, https://doi.org/10.1175/2010JAS3541.1.

Mlawer, E. J., S. J. Taubman, P. D. Brown, M. J. Iacono, and S. A. Clough, 1997: Radiative transfer for inhomogeneous atmospheres: RRTM, a validated correlated-k model for the longwave. *J. Geophys. Res.*, **102**, 16 663–16 682, https://doi.org/10.1029/97JD00237.

Morrison, H., and J. Milbrandt, 2011: Comparison of two-moment bulk microphysics schemes in idealized supercell thunderstorm simulations. *Mon. Wea. Rev.*, **139**, 1103–1130, https://doi.org/10.1175/2010MWR3433.1.

——, G. Thompson, and V. Tatarskii, 2009: Impact of cloud microphysics on the development of trailing stratiform precipitation in a simulated squall line: Comparison of one- and two-moment schemes. *Mon. Wea. Rev.*, **137**, 991–1007, https://doi.org/10.1175/2008MWR2556.1.

——, S. A. Tessendorf, K. Ikeda, and G. Thompson, 2012: Sensitivity of a simulated midlatitude squall line to parameterization of raindrop breakup. *Mon. Wea. Rev.*, **140**, 2437–2460, https://doi.org/10.1175/MWR-D-11-00283.1.

——, J. A. Milbrandt, G. H. Bryan, K. Ikeda, S. A. Tessendorf, and G. Thompson, 2015: Parameterization of cloud microphysics based on the prediction of bulk ice particle properties. Part II: Case study comparisons with observations and other schemes. *J. Atmos. Sci.*, **72**, 312–339, https://doi.org/10.1175/JAS-D-14-0066.1.

Muradyan, P., and R. Coulter, 1998: Radar Wind Profiler (915RWPPRECIPMOM) (12 June 2011). Southern Great Plains (SGP) Central Facility, Lamont, OK (C1), Atmospheric Radiation Measurement (ARM) Climate Research Facility, Oak Ridge, TN, accessed 27 January 2012, https://doi.org/10.5439/1025128.

Planche, C., W. Wobrock, and A. I. Flossmann, 2014: The continuous melting process in a cloud-scale model using a bin microphysics scheme. *Quart. J. Roy. Meteor. Soc.*, **140**, 1986–1996, https://doi.org/10.1002/qj.2265.

——, F. Tridon, S. Banson, G. Thompson, M. Monier, A. Battaglia, and W. Wobrock, 2019: On the realism of the rain microphysics representation of a squall line in the WRF Model. Part II: Sensitivity studies on the rain drop size distributions. *Mon. Wea. Rev.*, **147**, 2811–2825, https://doi.org/10.1175/MWR-D-18-0019.1.

Potvin, C. K., A. Shapiro, and M. Xue, 2012: Impact of a vertical vorticity constraint in variational dual-Doppler wind analysis: Tests with real and simulated supercell data. *J. Atmos. Oceanic Technol.*, **29**, 32–49, https://doi.org/10.1175/JTECH-D-11-00019.1.

Ryzhkov, A. V., 2007: The impact of beam broadening on the quality of radar polarimetric data. *J. Atmos. Oceanic Technol.*, **24**, 729–744, https://doi.org/10.1175/JTECH2003.1.

Shapiro, A., C. K. Potvin, and J. Gao, 2009: Use of a vertical vorticity equation in variational dual-Doppler wind analysis. *J. Atmos. Oceanic Technol.*, **26**, 2089–2106, https://doi.org/10.1175/2009JTECHA1256.1.

Skamarock, W. C., and Coauthors, 2008: A description of the Advanced Research WRF version 3. NCAR Tech. Note NCAR/TN-475+STR, 113 pp., https://doi.org/10.5065/D68S4MVH.

Smith, P. L., 1984: Equivalent radar reflectivity factors for snow and ice particles. *J. Climate Appl. Meteor.*, **23**, 1258–1260, https://doi.org/10.1175/1520-0450(1984)023<1258:ERRFFS>2.0.CO;2.

Testud, J., S. Oury, R. A. Black, P. Amayenc, and X. Dou, 2001: The concept of ''normalized'' distribution to describe raindrop spectra: A tool for cloud physics and cloud remote sensing. *J. Appl. Meteor. Climatol.*, **40**, 1118–1140, https://doi.org/10.1175/1520-0450(2001)040<1118:TCONDT>2.0.CO;2.

Thompson, G., P. R. Field, R. M. Rasmussen, and W. D. Hall, 2008: Explicit forecasts of winter precipitation using an improved bulk microphysics scheme. Part II: Implementation of a new snow parameterization. *Mon. Wea. Rev.*, **136**, 5095–5115, https://doi.org/10.1175/2008MWR2387.1.

Tian, L., G. M. Heymsfield, L. Li, and R. C. Srivastava, 2007: Properties of light stratiform rain derived from 10- and 94-GHz airborne Doppler radars measurements. *J. Geophys. Res.*, **112**, D11211, https://doi.org/10.1029/2006JD008144.

Tridon, F., and A. Battaglia, 2015: Dual-frequency radar Doppler spectral retrieval of rain drop size distributions and entangled dynamics variables. *J. Geophys. Res. Atmos.*, **120**, 5585–5601, https://doi.org/10.1002/2014JD023023.

——, J. Van Baelen, and Y. Pointin, 2011: Aliasing in micro rain radar data due to strong vertical winds. *Geophys. Res. Lett.*, **38**, L02804, https://doi.org/10.1029/2010GL046018.

——, A. Battaglia, and P. Kollias, 2013a: Distengling Mie and attenuation effects in rain using a K_a–W dual-wavelength Doppler spectral ratio technique. *Geophys. Res. Lett.*, **40**, 5548–5552, https://doi.org/10.1002/2013GL057454.

——, ——, ——, E. Luke, and C. R. Williams, 2013b: Signal postprocessing and reflectivity calibration of the atmospheric radiation measurement program 915-MHz wind profilers. *J. Atmos. Oceanic Technol.*, **30**, 1038–1054, https://doi.org/10.1175/JTECH-D-12-00146.1.

——, ——, E. Luke, and P. Kollias, 2017a: Rain retrieval from dual-frequency radar Doppler spectra: Validation and potential for a midlatitude precipitating case-study. *Quart. J. Roy. Meteor. Soc.*, **143**, 1364–1380, https://doi.org/10.1002/qj.3010.

——, ——, and D. Watters, 2017b: Evaporation in action sensed by multiwavelength Doppler radars. *J. Geophys. Res. Atmos.*, **122**, 9379–9390, https://doi.org/10.1002/2016JD025998.

Turner, D. D., and J. E. M. Goldsmith, 1999: Twenty-four-hour Raman lidar water vapor measurements during the

Atmospheric Radiation Measurement Program's 1996 and 1997 water vapor intensive observation periods. *J. Atmos. Oceanic Technol.*, **16**, 1062–1076, https://doi.org/10.1175/1520-0426(1999)016<1062:TFHRLW>2.0.CO;2.

——, R. A. Ferrare, L. A. H. Brasseur, W. F. Feltz, and T. P. Tooman, 2002: Automated retrievals of water vapor and aerosol profiles from an operational Raman lidar. *J. Atmos. Oceanic Technol.*, **19**, 37–50, https://doi.org/10.1175/1520-0426(2002)019<0037:AROWVA>2.0.CO;2.

——, J. E. M. Goldsmith, and R. A. Ferrare, 2016: *Development and Applications of the ARM Raman Lidar. Meteor. Monogr.*, No. 57, Amer. Meteor. Soc., 18.1–18.15, https://doi.org/10.1175/AMSMONOGRAPHS-D-15-0026.1.

Uijlenhoet, R., M. Steiner, and J. A. Smith, 2003: Variability of raindrop size distributions in a squall line and implications for radar rainfall estimation. *J. Hydrometeor.*, **4**, 43–61, https://doi.org/10.1175/1525-7541(2003)004<0043:VORSDI>2.0.CO;2.

Van Weverberg, K., A. M. Vogelmann, H. Morrison, and J. A. Milbrandt, 2012: Sensitivity of idealized squall-line simulations to the level of complexity used in two-moment bulk microphysics schemes. *Mon. Wea. Rev.*, **140**, 1883–1907, https://doi.org/10.1175/MWR-D-11-00120.1.

Varble, A., and Coauthors, 2014a: Evaluation of cloud-resolving and limited area model intercomparison simulations using TWP-ICE observations: 1. Deep convective updraft properties. *J. Geophys. Res. Atmos.*, **119**, 13 891–13 918, https://doi.org/10.1002/2013JD021371.

——, and Coauthors, 2014b: Evaluation of cloud-resolving and limited area model intercomparison simulations using TWP-ICE observations: 2. Precipitation microphysics. *J. Geophys. Res. Atmos.*, **119**, 13 919–13 945, https://doi.org/10.1002/2013JD021372.

Wacker, U., and A. Seifert, 2001: Evolution of rain water profiles resulting from pure sedimentation: Spectral vs. parameterized description. *Atmos. Res.*, **58**, 19–39, https://doi.org/10.1016/S0169-8095(01)00081-3.

Walko, R. L., W. R. Cotton, M. P. Meyers, and J. Y. Harrington, 1995: New RAMS cloud microphysics parameterization. Part I: The single-moment scheme. *Atmos. Res.*, **38**, 29–62, https://doi.org/10.1016/0169-8095(94)00087-T.

Williams, C. R., 2016: Reflectivity and liquid water content vertical decomposition diagrams to diagnose vertical evolution of raindrop size distributions. *J. Atmos. Oceanic Technol.*, **33**, 579–595, https://doi.org/10.1175/JTECH-D-15-0208.1.

——, and Coauthors, 2014: Describing the shape of raindrop size distributions using uncorrelated raindrop mass spectrum parameters. *J. Appl. Meteor. Climatol.*, **53**, 1282–1296, https://doi.org/10.1175/JAMC-D-13-076.1.

Wilson, D. R., and S. P. Ballard, 1999: A microphysically based precipitation scheme for the UK Meteorological Office Unified Model. *Quart. J. Roy. Meteor. Soc.*, **125**, 1607–1636, https://doi.org/10.1002/qj.49712555707.

——, A. J. Illingworth, and T. M. Blackman, 1997: Differential Doppler velocity: A radar parameter for characterizing hydrometeor size distributions. *J. Appl. Meteor.*, **36**, 649–663, https://doi.org/10.1175/1520-0450-36.6.649.

Xue, L., and Coauthors, 2017: Idealized simulations of a squall line from the MC3E field campaign applying three bin microphysics schemes: Dynamic and thermodynamic structure. *Mon. Wea. Rev.*, **145**, 4789–4812, https://doi.org/10.1175/MWR-D-16-0385.1.